Memoirs of the Faculty of Science, Kyoto University, Series of Physics, Astrophysics, Geophysics and Chemistry, Vol. XXXVII, No. 2, Article 3, 1988

Method of Digital Surface Photometry of Galaxies and Its Application to the Edge-on Galaxy NGC 5907

By

Toshiyuki SASAKI*

Department of Astronomy, Faculty of Science, University of Kyoto

(Received March 18, 1987)

Abstract

A method of digital surface photometry of galaxies has been developed to achieve the accurate photometry of the faint outskirt of the galactic disk. The method includes the stack of photographic plates to increase the signal to noise ratio of the data. Performance test of the measuring instrument Joyce-Loebl MDM6 and the procedures of digital surface photometry are fully described. The procedures are applied to the edge-on Sc galaxy NGC 5907 with a particular intention to reveal optical warping of the outer disk. Seven and eight deeply-exposed photographic plates in blue (J) and red (F) color bands, respectively, are analyzed. The photometry is carried out down to the faintest level of 27.64 J mag arcsec^{-2} (1 σ). The photometric accuracy of 0.04 mag at levels brighter than 24.5 J mag arcsec^{-2} and 0.46 mag at the faintest level is achieved after stacking plates. The photometric data of NGC 5907 are presented in the de Vaucouleurs' system in tabular form.

1. Introduction

Digital surface photometry of photographic plates has been developed largely during recent decades in accordance with developments of electronic computers and measuring engines such as PDS microdensitometer and Joyce-Loebl's. These facilities made it possible for us to measure and analyze photographic plates of large size with high speed and accuracy. de Vaucouleurs and his collaborators established reduction methods for digital surface photometry of galaxies and showed the capability and versatility of their procedures. Since then many investigators have developed the procedures to yield the accurate photometry down to 26 mag arcsec^{-2} (Jones et al. 1967; Ables 1971; Simkin 1975; Schweizer 1976; Arp and Lorre 1976; Barbon et al. 1976; Benedict 1976; Kormendy 1977; Okamura 1977; Fraser 1977; Tsikoudi 1977; Pence 1978; Strom and Strom 1978; Blackman 1979; Burstein 1979; van der Kruit 1979; Boroson 1981; also see proceedings of the conference at Triest edited by Sedmak et al. 1979 and at Toulouse by Nieto 1984, and the bibliography by Davoust and Pence 1982), or to even fainter levels for a large sample of galaxies (Watanabe 1982; Binggeli et al. 1984, 1985).

*) Present address: Okayama Astrophysical Observatory, Tokyo Astronomical Observatory, University of Tokyo, Kamogata-chou, Asakuchi-gun, Okayama 719-02

A troublesome aspect of doing photographic surface photometry, however, is that the largest errors are mostly systematic ones in nature, introduced in the various stages of data reduction. Errors of photographic surface photometry of each plate typically amount up to three percent of the sky brightness. We can reduce the errors and improve the quality of images by stacking digital images (see for examples Arp 1977; Lorre 1978). This procedure corresponds (1) to increasing the integration time of signal photons from astronomical objects up to an amount which cannot be allowed for one photographic plate due to saturation and (2) to reducing random errors and some systematic errors specific for individual plates.

Capaccioli and de Vaucouleurs (1983) discussed sources of accidental and systematic errors in the surface photometry of galaxies at low surface brightness levels. They showed that various sources of errors restrict the range of the meaningful surface-photometric data to $\mu_B \leqq 28$ mag arcsec^{-2}, where μ_B is the surface brightness in B band. Photometric accuracy higher than 0.1 mag is difficult to achieve even at brighter levels, $18 \leqq \mu_B < 28$. In the present study we develop a reduction system to process photographic images and stack them in order to achieve high accuracy down to the 28 mag arcsec^{-2} level.

The galaxy NGC 5907 is a nearly edge-on, bright galaxy with the morphological type SA(s)c:sp (de Vaucouleurs et al. 1976, hereafter abbreviated as RC2). It manifests the conspicuous warp in the outer HI disk (Sancisi 1976). van der Kruit (1979) tried to detect the optical warp in NGC 5907 by stacking two deeply-exposed plates taken at the Palomer 48 inch Schmidt telescope, and succeeded in detecting hints of warping of the optical disk in the profiles of the outer part of the galaxy around the levels of 26 mag arcsec^{-2}. The reduction procedures of the surface photometry are applied to NGC 5907 in order to settle the question whether there exists the optical warp or not in this galaxy.

We would obtain images of astronomical objects by using the two-dimensional electronic devices such as CCD to perform photometry with high efficiency and accuracy. However, a size of photosensitive area of CCD is small relative to the image of NGC 5907 of about 14 arcmin even on the telescope with a short focal length like the Kiso Schmidt telescope. A photographic plate is a useful detector to investigate the extended objects like our target galaxy, unless we can match the size of CCD detectors with that of the object by using a focal reducer and so on.

In this paper we describe the procedures of measurement of photographic plates and the reduction system of digitized data, together with the analysis of errors introduced in the reduction processes. Procedures of photographic observations of NGC 5907 are described in secton 2. A performance test on the measuring machine Joyce-Loebl MDM6 is described in section 3. Digitized densities of plates are processed and reduced by the method desribed in section 4. Internal and external errors are analyzed in section 5. Surface photometry of NGC 5907 is carried out in section 6. In section 7, we briefly summarize the reduction procedures and the accuracy of digital surface photometry of the galaxy.

2. Observations

We intended to take photographs as deep as possible of the galaxy NGC 5907 which has a size of about 14 arcmin. Observations were done using the 105 cm Schmidt telescope at the Kiso Observatory, a branch of the Tokyo Astronomical Observatory (Takase et al. 1977). The seeing size of stellar images is usually 2 to 3 arcsec at the Kiso Observatory which is a slightly larger than the image size defined by the optics of the Kiso telescope. Accurate photometry near the center of galaxies suffers under the lack of the spatial resolution but has no problem in the outer parts of the galaxy in this concern. Published data on the night-sky brightness at the Kiso Observatory indicate that the contamination of the city light is about 23.6 V mag arcsec^{-2}, that is, 21 percent of the sky brightness 21.9 V mag arcsec^{-2} in Kiso (Ishida 1978). The Kodak emulsion of type IIIa–J cuts off the wavelength region which includes the strong airglow emission of [OI] at λ 5577 Å and the city-light of Hg at λ 5461 Å. The strong Hg emission lines at λ 4348 Å and λ 4358 Å can be excluded by using the sharp-cut filter Schott GG455. We adopted the combination of the emulsion and the filter, IIIa–J+GG455, with the passband of $\lambda\lambda$ 4600 Å–5400 Å (J band).

Each plate was hypersensitized by being baked in forming gas. The conditions of the hypersensitization were decided to give the maximun gain in the detective quantum efficiency, DQE (Sasaki 1983; Aoki 1982). The quantity DQE is defined as

$$DQE = (S/N)_{out}^2/(S/N)_{in}^2, \tag{1}$$

where $(S/N)_{out}$ and $(S/N)_{in}$ mean the output signal-to-noise ratios and those of the incident radiation. This relation can be expressed in the photographic terms of exposure E, granularity σ_D, and contrast γ. Since $(S/N)_{out}$ is expressed as

$$(S/N)_{out} = \frac{0.4343\gamma}{\sigma_D}, \tag{2}$$

and $(S/N)_{in}$ is proportional to $E^{1/2}$, we obtain a relation

$$DQE \propto \frac{\gamma^2}{\sigma_D^2}\frac{1}{E}. \tag{3}$$

Plates were used immediately after exposure to the atmoshere after hypersensitization, because the gains achieved in hypersensitization would rapidly decrese with the time elapsed after exposure of the plates to the atmosphere (Sasaki 1983). Calibration step wedges were exposed on the four corners of the plate immediately after the end of the main exposure. Plates were developed for 5 min in the D–19 developer at 20°C.

In order to study the distribution of photometric color in the galaxy, in addition to the J color band, we used an emulsion and filter combination, IIIa–F +Schott RG610, which has their sensitibity to light in the range $\lambda\lambda$ 6100Å–6900Å (F band). The IIIa–F plates were treated in the same way as the IIIa–J.

A list of plates which were used in this analysis is given in table 1. Numerals in columns 6 and 7 of the table indicate the seeing sizes estimated by eye at observation and FWHMs of stellar images. We estimate the value of FWHM by fitting a gaussian

Table 1. List of

Plate (1)	Emulsion (2)	Filter (3)	Date (4)	Exposure (min) (5)
KL2656	IIIa-J*	GG455	Feb. 19,1980	208
KL2663	IIIa-J*	GG455	Feb. 20,1980	210
KL3204	IIIa-J	GG455	Mar. 10,1981	140
KL3211	IIIa-J	GG455	Mar. 11,1981	140
KL3314	IIIa-J	GG455	May 30,1981	70
KL3315	IIIa-J	GG455	Jun. 2,1981	110
KL3316	IIIa-J	GG455	Jun. 2,1981	140
KL3660	IIIa-F	RG610	Mar. 2,1982	96
KL3662	IIIa-F	RG610	Mar. 3,1982	120
KL3663	IIIa-F	RG610	Mar. 3,1982	30
KL3707	IIIa-F	RG610	Mar. 28,1982	105
KL3713	IIIa-F	RG610	Mar. 29,1982	115
KL3715	IIIa-F	RG610	Mar. 29,1982	115
KL3716	IIIa-F	RG610	Apr. 1,1982	120
KL3771	IIIa-F	RG610	May 23,1982	110

*Hypersensitization conditions were different from those of the other plates.

function to the stellar images by the least squares method (see in section 4). The densities at the sky level are given in column 8. In column 9 $(S/N)_{out}$ of each plate is indicated for the sky level together with the maximum $(S/N)_{out}$. Among these plates there is a short-exposure one in each color band, which we used to supplement the data of the saturated area around the very center of the galaxy in deep photographs.

3. Measuring instrument

Photographic plates were measured with a Joyce-Loebl microdensitometer MDM6 at the Department of Astronomy, University of Kyoto. This two-dimensional measuring machine is provided with two beams which are measured by two different photodiodes. Measured densities are digitized by 10 bits AD converter to be transferred to a minicomputer Data General NOVA 4/C. The minicomputer controls the whole MDM6 system and stores the digitized data in an 800 BPI magnetic tape. The machine MDM6 has two selectable measuring speeds; a standard full-step mode (5 mm sec^{-1}) and a half-step mode (2.5 mm sec^{-1}). We prepared control programs for raster scanning, for measuring calibration spots or step wedges, and also for the test of the stability of the machine. Data were monitored at the real time during raster scanning by the print-out of the average densities on an electric typewriter. When the calibration spots were measured, the program calculated the standard deviation of the micro noise level σ_D (Furenlid 1978) by

$$\sigma_D^2 = \sum_{i=2}^{N} (D_i - D_{i-1})^2/2(N-1), \tag{4}$$

to estimate the values of $(S/N)_{out}$ and DQE. Plates defects were removed automatically in the measuring procedure of the calibration spots.

plates used

Seeing Eye-estimated (arcsec) (6)	FWHM (arcsec) (7)	Sky density above fog (diffuse D.) (8)	S/N sky/max (9)	Note (10)
6	6.9	0.45	44/50	
4	8.8	0.57	49/54	
5	7.4	0.82	45/46	
2	4.0	0.61	40/49	
2	5.2	0.32	31/55	short exp.
3	6.2	0.67	40/45	
5	5.8	0.65	43/48	
5	7.4	0.59	32/43	
3	6.0	0.91	44/45	
3	6.2	0.17	19/47	short exp.
2	4.1	0.56	35/46	
2	4.2	0.68	38/42	
3	4.1	0.74	42/45	
4	6.4	0.79	40/41	
3	4.4	0.71	47/49	

The double-beam, compensated systems are prefered for surface photometry of galaxies to an uncompensated, single-beam instrument (Capaccioli and de Vaucouleurs 1983). The measuring machine, however, can introduce a significant amount of random and systematic errors, depending upon its performance. We carried out the performance test on MDM6 in order to take the results into account in the succeeding analyses. It is noted that densities are given in unit of specular density measured with MDM6 through this section. Conversion coefficients of the specular densities to the standard diffuse ones are given in section 3-5.

3-1. Stability

We measured the density at a point on a test piece of plate for 1000 times every 1.5 min in order to test the stability of the machine. The slit size was set to the same as the one used at the measurements of the galaxy. The upper panel of figure 1 shows the change in the recorded density against the time elapsed after the power was turned on. Although the machine was stabilized within 0.013 D after 3 hours of warming-up in one case, some oscillations with an amplitude of 0.013 D and with a period of 30 min lasted. In another case, such oscillations did not appear and the machine achieved the good stability with fluctuations much less than 0.01 D, though it needed 6 hours of the warming-up period. In most cases MDM6 was stable within 0.01 D after the warming-up of 3 hours.

A halogen lamp is used as a light source of MDM6. The lamp goes to dim out rapidly after a certain burn-out time (nearly 100 hours). The lower panel of figure 1 shows the rapid change of density when the lamp was going to run out. As it could be detected easily, we changed the lamp in time to avoid unusable measurements.

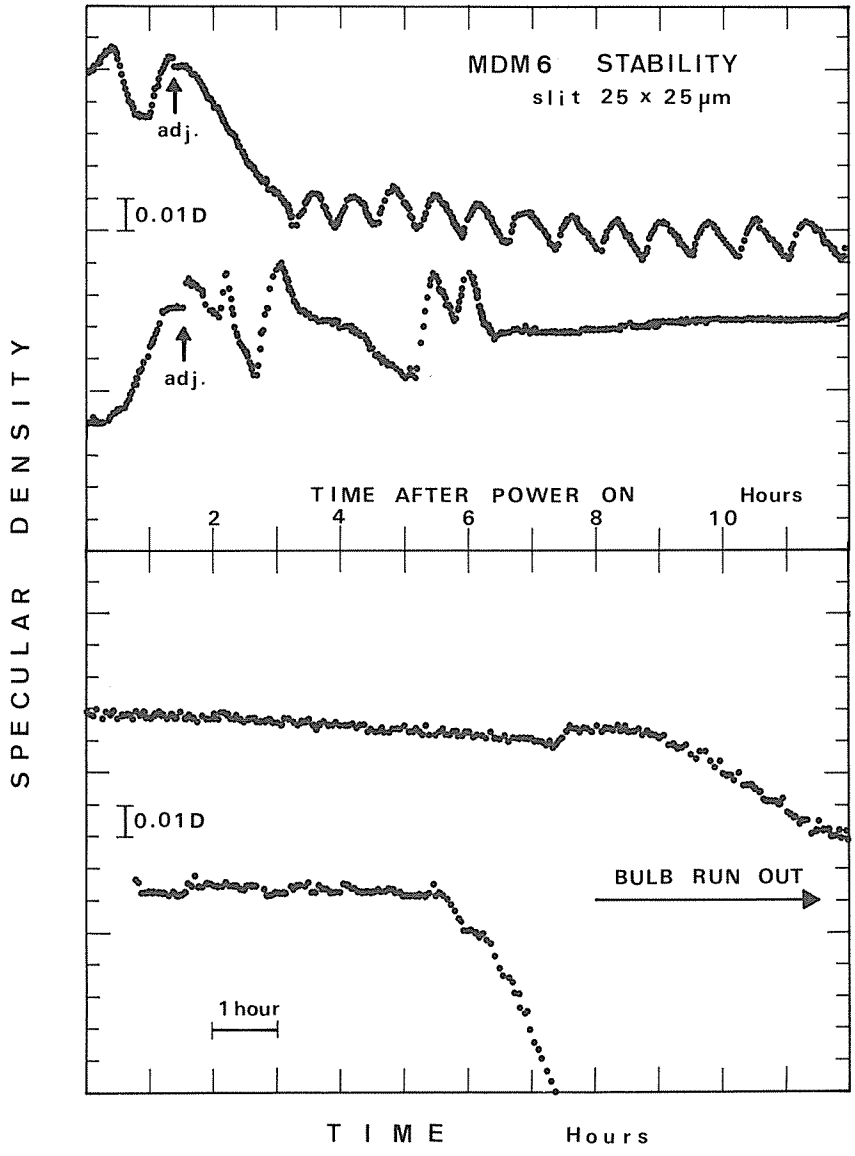

Figure 1. Stability of recorded specular density measured with the Joyce-Loebl microdensitometer MDM6. Each point is a mean of 1000 measurements at a particular point on the plate with the measuring table fixed using the same slit as that used in measuring object plates. The above panel shows the stability in the initial state just after the power was turned on. Focus adjustment caused fictitious jumps. Three hour warming-up was usually enough but some fluctuations with the amplitude of 0.013 D were remained in one case and a longer warming-up was needed in another case. The lower panel shows changes of recorded densities during the light source running out. The rapid changes in density were detected during then.

3-2. *Repeatability of Density Measurements*

We selected several plates with various densities, and each of several positions on the plates was measured 3000 times. Their mean densities and r.m.s. deviations were calculated. The latter serves as a measure of repeatability. The results are $\pm 0.003\ D$ for density less than 2.0 D, $\pm 0.007\ D$ for 2 to 3 D, and $\pm 0.020\ D$ for density greater than 3.0 D. These values, combined with the contrast of the IIIa-type emulsion $\gamma \sim 3$, correspond to fluctuations of a relative intensity less than 1.5 percent, which are comparable to or less than granularity noises in a plate (see section 4-2).

3-3. *Positional Repeatability and Spread Functions*

A knife edge was set on the measuring table to produce the edge pattern. The table was moved back and forth over 20 cm at the speed of full step mode. Typical traces of the knife edge are shown in figure 2 in directions of X and Y axes. There were systematic differences in the recorded positions of the knife edge between normal scans and reverse scans. These differences were about 15 μm in X and 20 μm in Y irrespective to the table speed and are caused due to the backlash. However, the raster scan permits movement of the table only along one direction both in X and Y. When the scan is limited to one direction, the recorded positions of the edge coincide within 2 μm for several scans along each axis.

The machine MDM6 measures the position by converting steps of stepping motors directly to coordinates. Certain differences between real and calculated coordinates occur especially near the starting and stopping points where a motor needs to produce a torque larger than in the normal scanning. When the table was set backward for a distance more than 100 μm from the knife edge and then set to run foreward, the

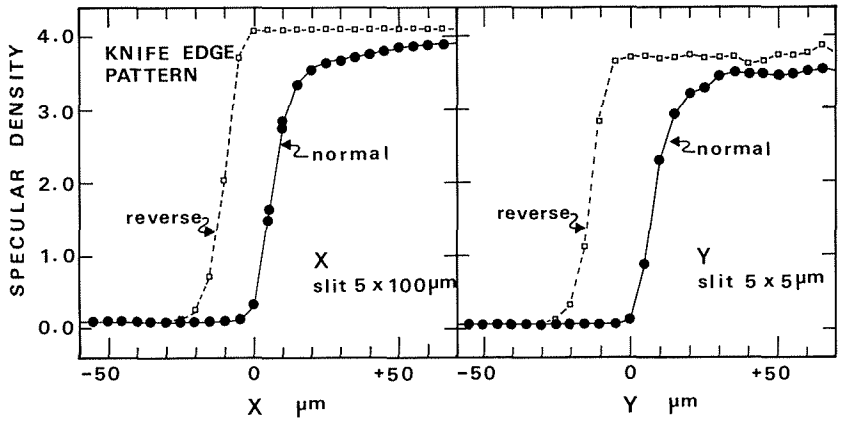

Figure 2. Response of MDM6 at the abrupt change of density at a knife edge. The knife edge was measured with slits of the narrowest width available in the direction of the table scan and with the maximum area. MDM6 cannot follow the abrupt change of density from the transparent to the opaque part. There are systematic differences in detected positions of the knife edge between the normal and its reverse scans. Some fluctuations in opaque parts in Y scans are caused by insufficient light due to the small slit used.

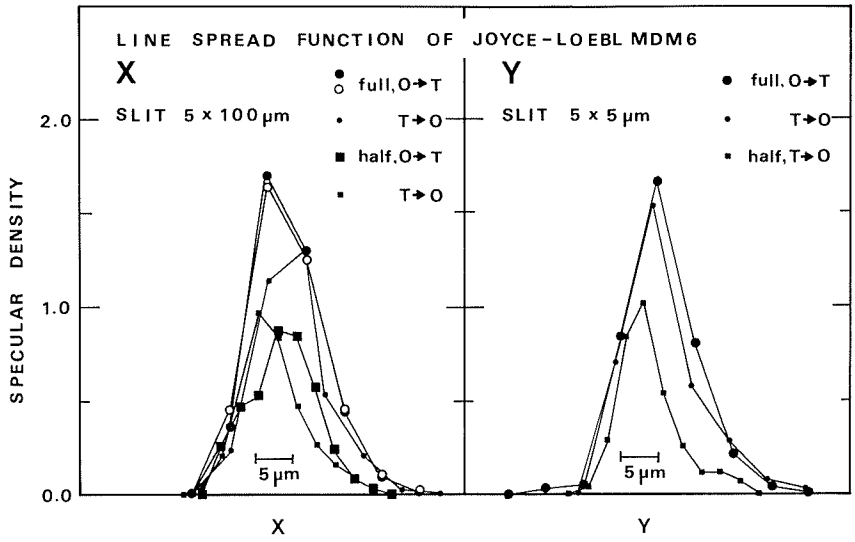

Figure 3. Line spread functions of MDM6 along the X and Y axes. Measurements were the same as used in figure 2; the scan from the opaque (O) to the transparent (T) part and its reverse scan with a full step (every 5 μm) and a half step (every 2.5 μm). FWHM was obtained of 10 μm for every case.

recorded positions of the edge showed no more anomaly.

When a normal scan ran through the knife edge from the transparent area to the opaque area, it turned out that measured densities at high values showed some difference between the normal and the reverse scans as seen in figure 2. The machine MDM6 cannot follow the steep density gradient such as the knife edge, though such a large gradient does not occur in the real astronomical measurements.

We can derive the line spread function from the knife-edge patterns (figure 3). The forms of the function are the same in both directions along the X and Y axes. The measuring table can move in two speeds, namely, the full step mode and the half step mode. The line spread functions differ in amplitude between the cases of different speeds, but possess the same FWHMs of 10 μm.

3-4. Orthogonality of Axes

We examined the orthogonality of the table axes by comparing the positions of marked images on the plate with those obtained after a rotation of 90°. The small angle of misalignment between the actual X and Y axes, θ_1, and the small difference of the angle of the actual rotation from 90°, θ_2, are related to the (X, Y) coordinates:

$$\begin{aligned} \theta_1-\theta_2 &= \quad (Y'-X)/Y\,, \\ \theta_1+\theta_2 &= -(X'+Y)/X\,, \end{aligned} \tag{5}$$

where (X', Y') are the coordinates of an image originally at (X, Y) after the rotation of 90°.

The departure from the orthogonality was found to be 0.021 degree ($\sin\theta_1 = 3.67\times10^{-4}$ and $1-\cos\theta_1 = 6.72\times10^{-8}$).

3-5. Calibration of Density Scale

Kodak Interobservatory Density Standard Wedges were prepared by the AAS Photographic Working Group (Sewell 1975; Smith and Hoag 1979). The standard wedges No. 34 at the Kiso Observatory were used for the calibration of our densitometer in the diffuse density scale.

The conversion coefficients of the specular densities to the standard diffuse densities are 0.817 ± 0.007 for Ia-type emulsion, 0.774 ± 0.016 for IIa-type, and 0.767 ± 0.014 for IIIa-type.

3-6. Influence of Depth of Focus

The depth of focus of the optics on MDM6 is about 2 μm after its specification. Photographic plates are not flat within this accuracy over the whole area. Furthermore plates are bent in the plate holder of the Kiso Schmidt telescope, and the hysteresis of this bending may remain. The short depth of focus influences measurements to a certain degree under these circumstances. Instead of measuring the plate distortion, we evaluated the density variations due to the change of the focus. According to our experiences in the surface photometry of the galaxy, the density variation may be less than 0.01 D over 15 mm $\times$ 18 mm area due to this effect.

The gradual focus change over the plates causes effects in density measurement comparable to those of the drift of the intrinsic density scale of the machine.

4. Measurement and Data Reduction

4-1. Measurement

Photographic plates were measured with the microdensitometer MDM6 described in the previous section. The performance test showed that it needs warming-up time typically for three hours. During the warming-up, we measured a certain point on the test piece of plate to monitor the system stability until the system became stable within ± 0.01 D. We have to measure plates over an area several times as large as those of the object itself in order to subtract the sky background by interpolation (Jones et al. 1967). The object galaxy NGC 5907 extends on the sky over 14×1.3 arcmin^2, which is 13.6×1.3 mm^2 on the plates taken with the Schmidt telescope at the Kiso Observatory (the plate scale is 62.592 arcsec mm^{-1}). We measured plates to obtain two separate frames, that is, a small, high-resolution, inner 'galaxy' frame and a large, low-resolution, outer 'sky' frame including the former frame, as shown in figure 4. The sky frame was measured with a large slit size of 250×250 μm^2 and scanning steps of 250 μm over 30×40 mm^2 area. The galaxy frame was scanned every 15 μm in X and Y with a 25×25 μm^2 slit over 15×18 mm^2 area. A scanning slit size nearly twice the scanning step was selected for the galaxy frame to reduce the noises. A total number of data amounted to 100 KB and 4 MB for the sky and the galaxy frames, respectively. It needed 30 min and 150 min to obtain them.

The calibration step wedges of each plate were measured for each frame. As the raster scan of the galaxy frame needed a relatively long time about 150 min, density records might fluctuate and/or drift, and the lamp might run out during the measure-

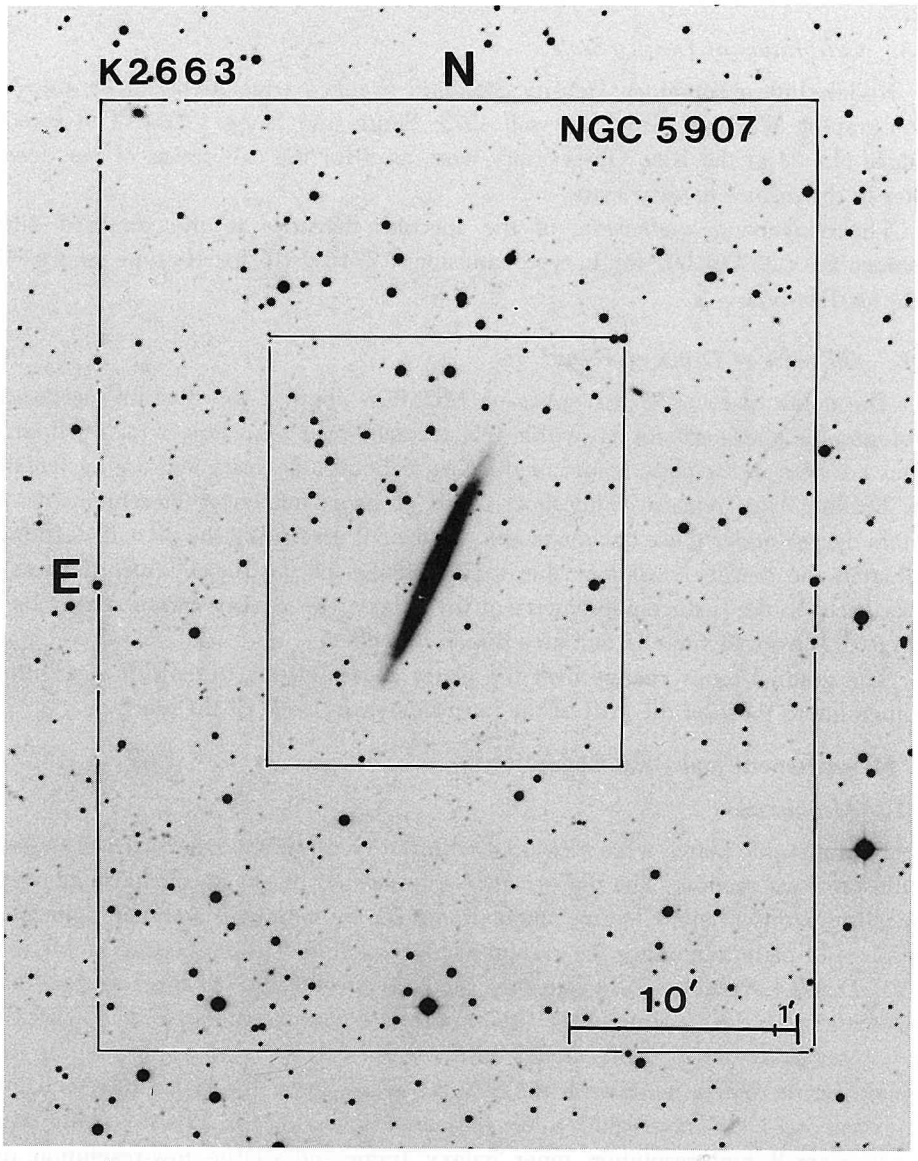

Figure 4. The warping edge-on galaxy NGC 5907. The plate KL2663 was taken with the 105 cm Schmidt telescope at the Kiso Observatory. Exposure was made on Kodak IIIa-J (hypersensitized) through Schott GG 455 for 210 min. The inner and outer squares superposed indicate areas for the galaxy and the sky-background frames, respectively.

ment. These events were examined after the measurement of each frame by using the scan of step wedges. Two wedges out of the four were measured at first before the scan of each frame, and were used to draw the characteristic curves. After the scan of the galaxy frame, the wedge which had been measured last before scan of the galaxy frame was measured again to examine the stability of the microdensitometer. Differences between recorded wedge densities of these subsequent measurements were less than 0.1

D for all cases, as expected from the performance test of MDM6. The sky frame was measured in almost the same way as the galaxy frame. After the completion of measurements of the galaxy and the sky frames in each plate at one stretch, the stability was again examined to check the power of the lamp and the whole system.

4–2. Transformation in Intensity Scale

Measured densities were converted into relative intensities with the help of a characteristic curve (HD curve). There exist several functional forms proposed to represent the characteristic curve (see de Vaucouleurs 1968). Tsubaki and Engvold (1975) proposed a formula which can reproduce characteristic curves of various types: Relative intensity, I, is represented in their method as

$$\log I = A_1 D + A_2 \ln(\exp(BD^{C1}) - 1) + A_3 \exp(BD^{C2}) + A_4 , \tag{6}$$

where D is density, $A's$, B, $C's$ are constant. Seven constants are determined iteratively by the non-linear least squares method.

When the density was converted into the relative intensity, the output signal-to-noise ratio $(S/N)_{out}$ was calculated for every pixel in the frame by equation (2). As we could not derive granularity σ_D from step wedges used, we obtained the dependence of σ_D on the density D by measuring many plates with various conditions of plate treatment, for such dependence cannot be influenced by any treatment of plates (Furenlid 1978). As seen in figure 5, σ_D to D relation is well represented both for IIIa–J and IIIa–F plates by straight lines except for the part of low densities. It is noted that σ_D depends on the density including the fog. Densities were measured with zero point defined by the level without a plate in the measuring beam.

Figure 6 shows examples of the characteristic curve, σ_D, and $(S/N)_{out}$ for the plate KL2663. Tsubaki and Engvold's formula was fitted with residuals in $\log I$ of typically 0.02, which are presented in column 2 of table 2. For several plates, the residuals were greater than 0.03. In these cases density scales were differed systematically between the two strips of step wedges measured due to unidentified cause.

4–3. Sky Background Subtraction

The contribution of the sky background including the fog was subtracted from the object data. The local fluctuations of the sensitivity of a plate, vignetting of the telescope optics and nonuniformity of the atmospheric transmission over the field can be eliminated when the data are normalized to the local sky background, which is obtained through interpolation of the sky data around the galaxy. Polynomial series were used to fit the intensity distribution of the sky background by the least squares method. There were stellar and small galaxy images and plate defects which we removed from each frame before fitting the sky intensity distribution. In order to remove the large images coarsely at first, we used a linear function of positions to fit the intensity distribution in the frame including all images, and then omitted pixels, together with the adjacent pixels, where the differences between the measured intensities and the linearly fitted sky level were greater than 2 σ. Here σ is an r.m.s. deviation in intensity in fitting the sky background. We repeated the same procedure but using the

Table 2. Characteristics of the surface photometry

Plate	Residual in fitting of the HD curve		Sky fitting sky frame		galaxy frame		Residual in fitting of positions	r.m.s. noise in the sky	Intensity ratio of the sky level
			Order	Residual	Order	Residual			
	Δlog I	(%)		(%)		(%)	(μm)	(%)	
(1)	(2)	(3)	(4)	(5)	(6)	(7)	(8)	(9)	(10)
KL2656	0.013	(3.1)	4	0.54	1	0.70	9.3	3.22	1.13
KL2663	0.005	(1.3)	2	0.55	1	0.58	10.5	2.72	0.81
KL3204	0.015	(3.6)	5*	0.45	0	0.56	—	3.11	—
KL3211	0.031	(7.4)	6*	0.57	0	0.64	3.7	3.31	0.98
KL3314	0.025	(6.0)	6	0.87	1	1.37	4.8	5.95	1.56
KL3315	0.022	(5.3)	3	0.56	1	0.68	4.4	2.94	1.38
KL3316	0.008	(1.8)	5*	0.53	1	0.63	5.4	3.24	1.31
KL3660	0.068	(17.0)	3	0.66	1	0.86	5.5	3.90	0.73
KL3662	0.017	(3.9)	4	0.49	1	0.59	5.3	2.97	—
KL3663	0.025	(5.9)	3	1.17	1	1.40	3.9	6.36	0.86
KL3707	0.058	(14.2)	2	0.78	1	0.83	3.7	3.47	0.71
KL3713	0.026	(6.1)	3	0.57	1	0.69	3.7	3.16	0.81
KL3715	0.029	(6.8)	6	0.55	1	0.65	3.8	3.01	0.88
KL3716	0.040	(9.6)	2	0.55	1	0.70	5.7	3.26	0.91
KL3771	0.062	(15.4)	3	0.47	1	0.62	7.0	3.10	1.26

*Sky-fitting procedure was slightly different from others.

second-order polynomials and the threshold level in intensity of 2.5 σ to remove the faint stellar images. The second-order polynomials was enough for this purpose because there was little difference between the 2nd- and the 3rd-order presentation of polynomials for the removal of images (figure 7). The procedure was done iteratively until the decrease in σ by one step became less than 20 percent of the previous one. Then the intensity distribution of the frame free from any images was fitted by polynomials of the order from the 0-th to higher, but less than the 8-th. This limiting order was obtained to suppress the artificial oscillation of the functional form in the area of the removed galaxy image (Jones et al. 1967). The r.m.s. deviations in fitting the sky background decreased as the order of the fitting polynomials increased, as seen in

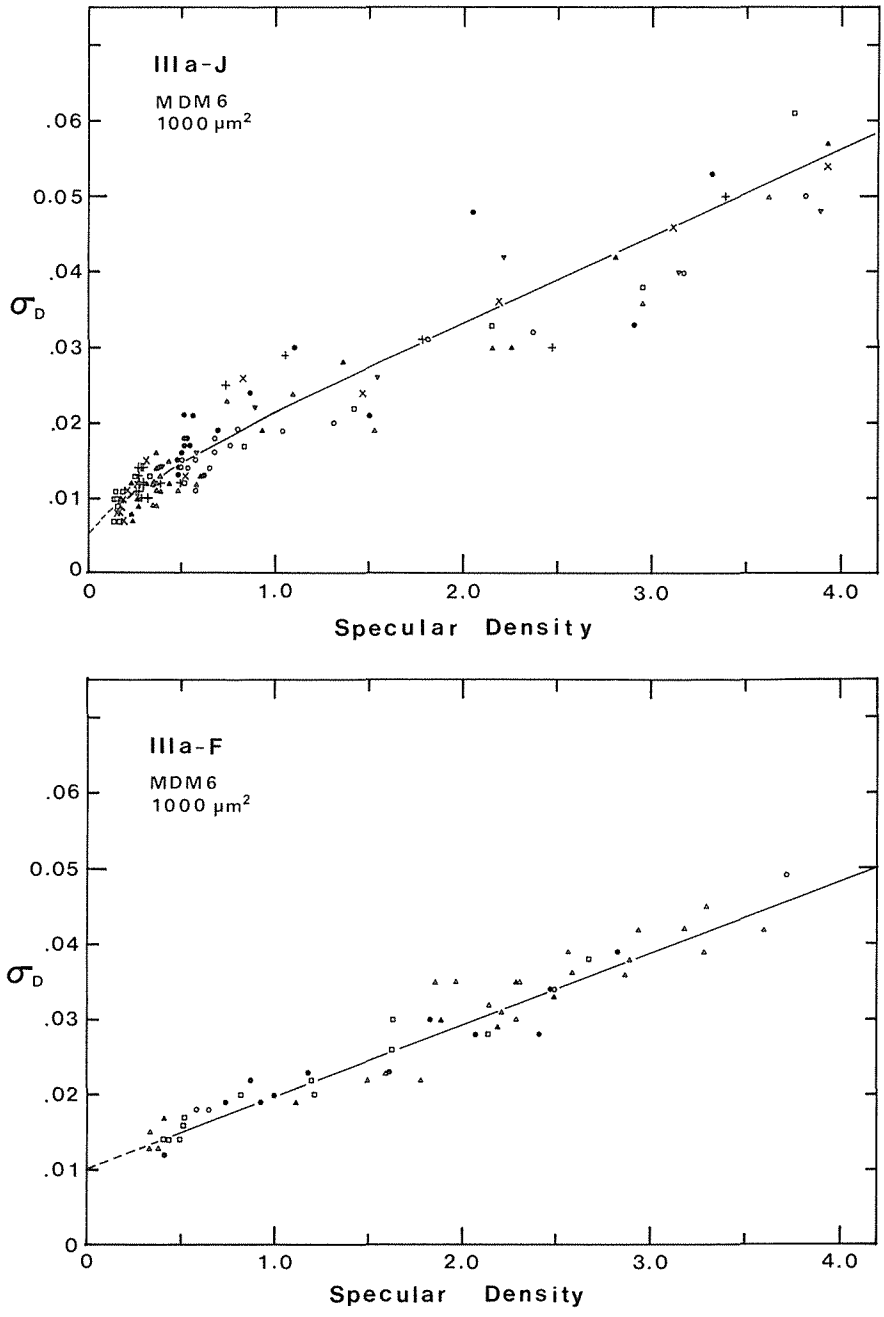

Figure 5. Granularity σ_D in specular density unit as a function of the density. σ_D was measured as the micro-noise by equation (4) from the total of 250 data points in the area of 500 $\times$500 μm^2 for IIIa-J plates, or the total of 1000 data points in the area of 1000 $\times$1000 μm^2 for IIIa-F plates. A slit of 10$\times$100 μm^2 (1000 μm^2) was used. The abscissa is the specular density including the gross fog. Different symbols correspond to different plates with various treatments. Straight lines indicate the mean relations adopted, which coincide nearly with those of Furenlid (1978).

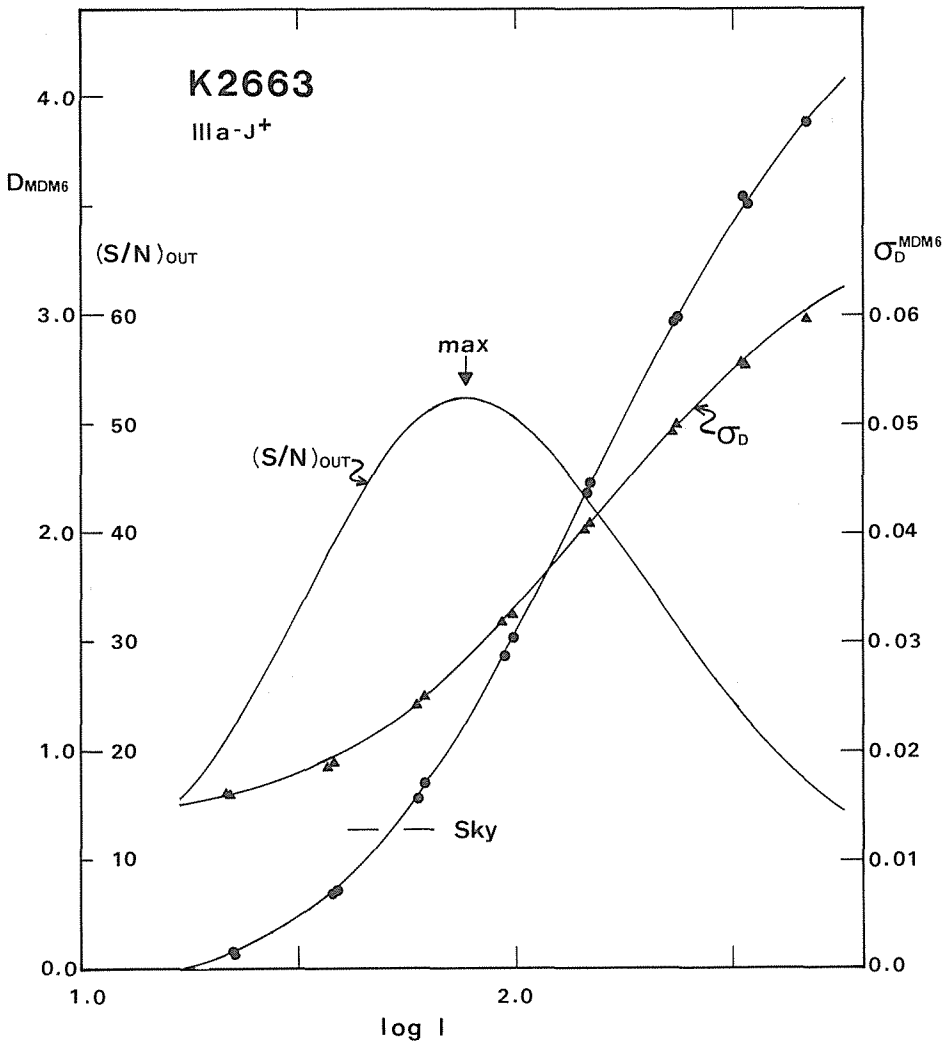

Figure 6. The characteristic curve and the distributions of granularity σ_D and output S/N of the plate KL2663. Densities are in unit of MDM6 specular density. The density at the sky level is indicated. The maximum output S/N is about 52.

figure 7. If the r.m.s. deviation in fitting was less than 20 percent of the previous deviation (less than 0.1 percent of the sky brightness) as the order increased, we completed the iteration of fitting procedures. Figure 8 illustrates the example of the intensity distribution of the sky background for the plate KL2663, superposed on a isointensity map. The orders of fitting polynomials are shown in column 4 of table 2. For three plates KL3204, KL3211, and KL3316, polynomials of the same order were used both for removal of images and for the fitting to the image-free data, and yielded residuals which little differed from the others as a result.

The local sky background intensities, I_S^*, expressed by the fitting polynomials were subtracted from the intensities in the galaxy frame, I_G, which were then devided

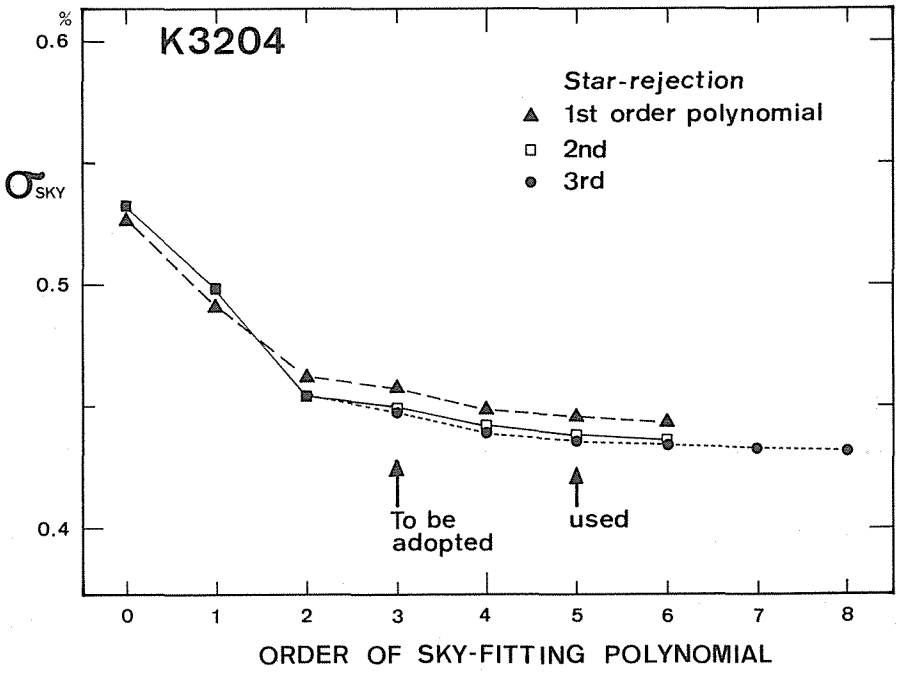

Figure 7. The r.m.s. deviations in intensity as a function of the order of the sky-fitting polynomial. Stellar images were removed by using the first- to third-ordered polynomials before the sky-fitting was applied. For data from the plate KL3204, the fifth-ordered polynomial was used for the sky-fitting, but the third order is enough with the same accuracy as those of other plates.

by the local sky intensities to yield the relative intensities

$$I_R(x, y) = \frac{I_G(x, y) - I_S^*(x, y)}{I_S^*(x, y)}. \tag{7}$$

The relative intensities were not yet free of errors due to the drift of the zero point of the measuring machine, the out-of-focus effects caused by the plate bending, and possible systematic differences in characteristic curves for separate measurements in the galaxy and the sky frames. We reduced these effects from the relative intensity in the galaxy frame, $I_R(x, y)$, by applying the same procedures of the removal of images and of fitting of the sky background as for the sky frame but with the 0-th or the 1st-order polynomials used, as shown in column 6 of table 2. The relative intensities corrected for the drift and others were then obtained as

$$I(x, y) = (I_R - I'_S)/(1 + I'_S), \tag{8}$$

where I'_S were the relative intensities of the local sky background determined in the galaxy frame of the relative intensities. The mean residual of all plates in the fitting process of the sky background was 0.62 percent of the sky brightness for the sky frame (column 5 of table 2) and the residual after the corrections for the drift and others for the galaxy frame became 0.77 percent of the sky brightness (column 7 of table 2).

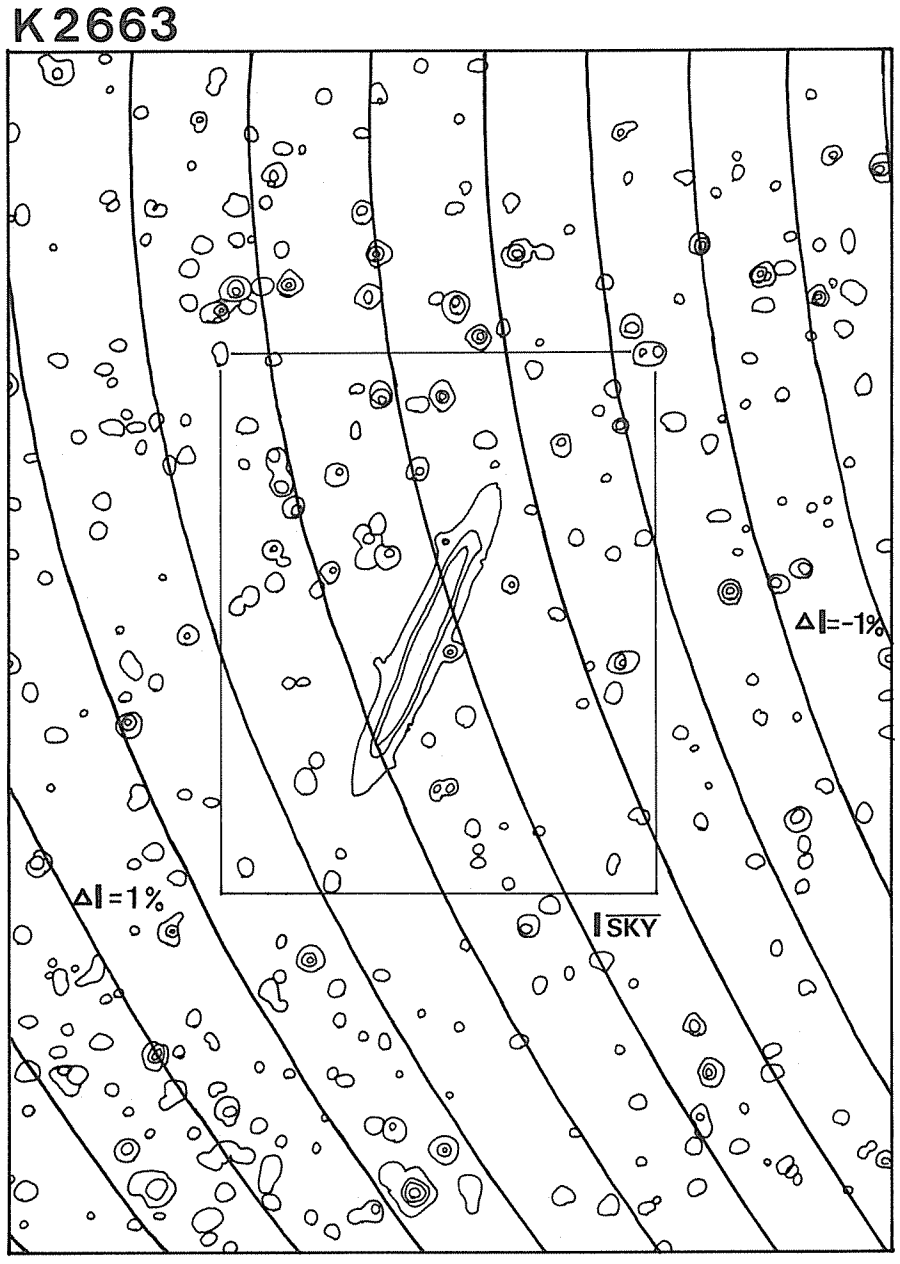

Figure 8. Distribution of intensity in the sky-background calculated with the fitted polynomials for the plate KL2663 plate. Thick lines indicate contours every 0.25% of the sky intensity, superposed by thin contour lines of stellar and galaxy images. An inner square shows the galaxy frame to be fully analyzed.

4-4. Position Fitting among Plates

We intended to stack plates as many as 7 plates in J band and 8 in F to improve the output signal-to-noise ratios. Although all plates were set on the measuring table of

MDM6 in the way as same as possible, but translations and a rotation of each frame were necessary to achieve an accurate positional fitting among them.

Stellar and nebular images were detected by an algorithm for "image pick-up" similar to one developed by Maehara (1981) in a procedure as follows: (1) A pixel with intensity greater by 3 σ than the sky intensity is considered as a part of one of object images. (2) Images already detected are examined to contain the pixel newly detected. (3) The pixel is added to one of the subsets of image pixels or stored as an independent image. (4) At the same time the contacting images are separated. (5) An image with a total number of pixels greater than 32 and spreads over more than two scanning steps is recorded.

For the detected images we calculated parameters such as centroids of images, total intensities, the pixel numbers, and mean intensities, and also recorded the peak intensities and (x, y) coordinates of the full extent of the images.

The total numbers of the images detected in the galaxy frames were about 120 and 140 for J and F plates, respectively. The images with a total number of pixels greater than 40 were used for the fitting procedure of the plate position onto that of the reference plate KL3204. The parameters involved in the translations and the rotation were derived by the least squares method and their residuals are shown in column 8 of table 2. A mean residual of the position-fitting was 5.5 μm, i.e., one third of the scanning step, which corresponds to 0.34 arcsec in the sky.

We translated and rotated the galaxy frames to the reference frame by applying the procedures described above. This translation process was inversely applied to the frame already translated to be compared with the original frame. The galaxy frame of KL3211 was processed to result in 4.0 μm r.m.s. Thus, we conclude that the procedures for the image pick-up and the translation were working accurately enough for our purposes.

4–5. Stack of Plates

We have now in hand the galaxy frames in intensity-scale relative to the sky brightness. The sky brightness varies day to day due to variable sky brightness (city light, airglow, and moonlight). The galaxy profiles in intensity were shifted to coincide each other to be corrected for the relative differences in the sky brightness. We first stacked plates by using this relative calibration, and the photoelectric calibration was applied for the galaxy data after the stacking.

The relative calibration was done with pixels in and around the galaxy which have a relative intensity greater than 0.2 (20 percent of the sky brightness) and $(S/N)_{out}$ greater than 40. Column 10 of table 2 shows the ratios of the sky brightness relative to that of the reference plate. As the quality of plates varies among plates used, a suitable weight were applied in the stacking. We adopted $(S/N)_{out}$ as a weight for each pixel. Arbitrary weights dependent on a exposure time were often used (Okamura 1977; Burstein 1979). The plate quality can be well represented by the value of $(S/N)_{out}$ when the faint level around the sky brightness is concerned. Burstein (1979) described that a weight proportional to the net signal-to-noise ratio gives a higher weight to the brighter part of the noise in the sky brightness, thus biasing the sky level. The value of $(S/N)_{out}$

is not so a strongly varying function of intensity at the sky level as the net S/N. The effect of difference in weights due to the noise in the sky brightness was estimated to be a shift of the sky level by less than 0.05 percent. We confirmed that the sky level, which was a little greater or less than the exact value of zero for each plate, substantially approached toward zero as plates were stacked.

The intensity of the stacked image, I_Σ, was calculated by

$$I_\Sigma(x, y) = \frac{\beta \Sigma w I}{\Sigma w}, \tag{9}$$

where $w=(S/N)_{out}$ and β is the ratio of the sky brightness with regard to the reference plate.

The suppression of noise is proportional to the square root of the number of plates stacked, as expected after the Poisson statics (table 3).

4-6. Smoothing

A typical noise level of our photographic plates was three percent of the sky brightness as seen in column 9 of table 2. Stacking reduced the noise down to 1.5 percent for the IIIa–J image (7 plates) and down to 1.2 percent for the IIIa–F image (8 plates) as shown in table 3. These noise levels correspond to 4.6 mag and 4.8 mag fainter than the sky brightness, respectively. We measured plates with a slit of a size larger than a scanning step (25 μm vs. 15 μm) to suppress the noise, because a typical grain size of IIIa type emulsion is about 10 μm. After we reduced the noise by stacking plates, we further suppressed the noise by smoothing data.

Gaussian-weighted smoothing was applied to each point in a galaxy frame with an extension of box area of the size twice an FWHM of the gaussian function. Values of the FWHM were 5 arcsec and 7 arcsec for the IIIa–J and the IIIa–F image, respectively. At the same time, the data size was compressed by one third. The smoothing largely reduced the noise level down to 0.5 percent of the sky brightness for IIIa–J and to 0.43 percent for IIIa–F, as shown in table 3. Gradual suppression of the noise level in the northern part of the galaxy is shown by bird's-eye views in figure 9. The right panel of figure 9 shows the final frame obtained after the gaussian smoothing. A bright star seen

Table 3. Noise suppression by stacking procedure

Emulsion (1)	No. of stacked plates (2)	r.m.s. noise in the sky (%) (3)	Estimated r.m.s. noise* (%) (4)	Stacked plates (5)
IIIa-J	4	2.05	1.58	3204, 3211, 3315, 3316
	7	1.46	1.26	all IIIa-J plates
IIIa-F	5	1.65	1.56	3662, 3713, 3716, 3771, 3663
	7	1.31	1.36	3660, 3662, 3663, 3707, 3713, 3716, 3771
	8	1.21	1.24	all IIIa-F plates

*Estimated from noises in the plates used except shortly-exposed plates KL3314(J) and KL3663(F).

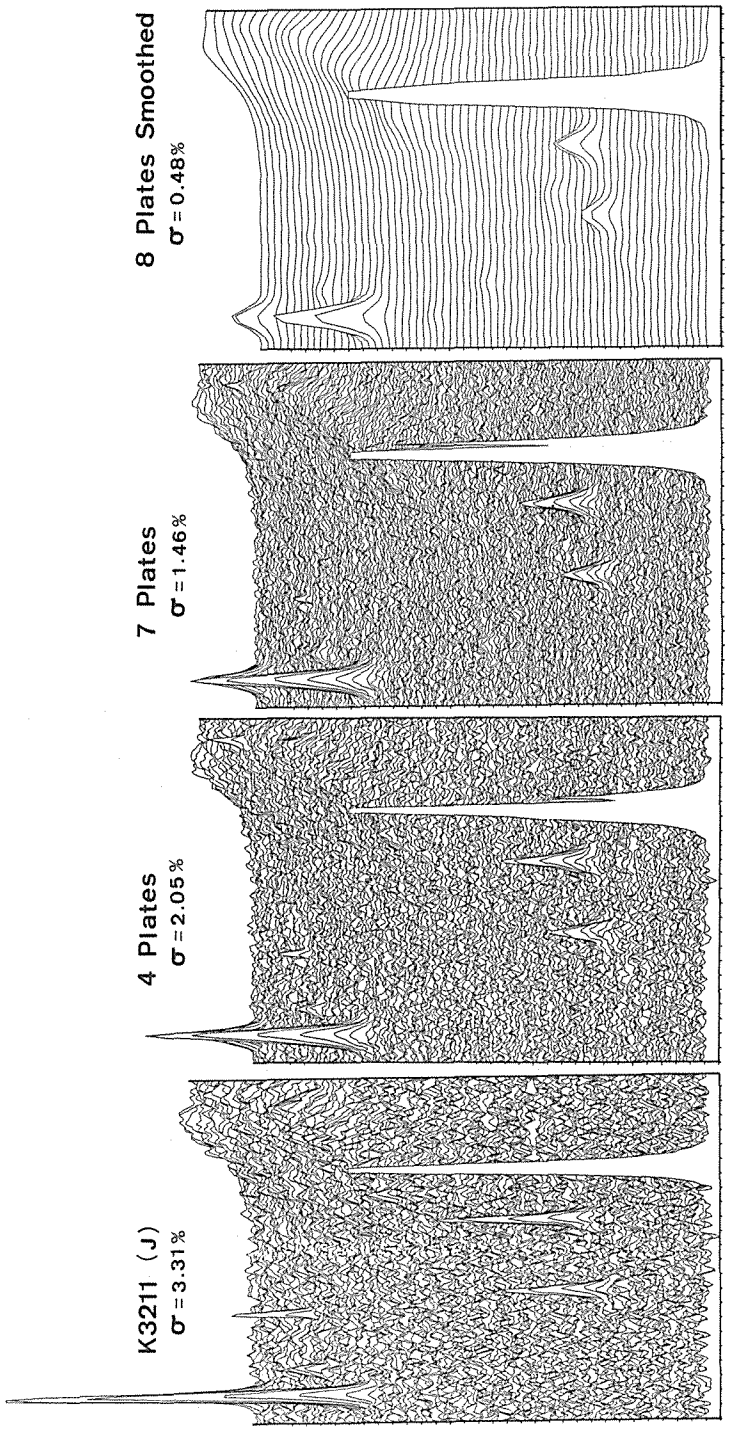

Figure 9. Perspectives of the distribution of intensity in the north-east region of the galaxy for IIIa-J plates. Reduction of noises can be seen from a single plate (left) through 4 plates and 7 plates stacked up to 8 plates smoothed after stacked (right). The r.m.s. fluctuations of the sky background are indicated. A bright star on the stacked data appears to be splitted due to different seeings and exclusion of the brightest portions with low *S/N* ratios. The data of 8 plates smoothed include those from the plate KL2789 which was not used in the present photometry due to a large defect near the main disk of the galaxy. The north is to the bottom and the east to the right.

in the northern portion of the figure has a fictitious spike in stellar profile in stacked frames, which was caused by exclusion of pixels with $(S/N)_{out}$ less than 40 in the stacking process. As the bright parts of the images are saturated, they possessed a low value of $(S/N)_{out}$ as seen in figure 6.

Finally we obtained the stacked galaxy frames in intensity relative to the sky brightness with the noise level suppressed down to 0.5 percent of the sky brightness.

4–7. Star Removal

To derive photometric parameters such as total intensity and color, stellar images were removed from the galaxy frames. Stellar images can be approximated by a gaussian function at least near their center (Capaccioli and de Vaucouleurs 1983; Kormendy 1973; Woolf 1982 and references cited therein). A two-dimensional gaussian profile was applied to stellar images in the galaxy frames. Background of the galaxy intensity was fitted by polynomials of the third order. Fitting of a stellar image and the background was performed simultaneously by the least squares method. Stellar images were removed from the frame and were replaced by the background represented with the third-order polynomials. Figure 10 shows the area free of stellar images by a box.

4–8. Profile of Stellar Images

Varying seeing has the greatest effects on the intensity distribution in areas with a large intensity gradients, such as in star images and in the central part of the galaxy. A color map would be influenced by the difference in image sizes between the stacked frames of two color bands. Particularly the color of the dust lane would be seriously affected. To avoid these effects, the difference in the image size was corrected: The frame with smaller image size was convolved by the two-dimensional gaussian point spread function to be matched to another frame with larger image size. The function

$$I(x, y) = A\exp\left\{\frac{-1}{2(1-\rho^2)}\left[\left(\frac{x-x_0}{\sigma_x}\right)^2 - 2\rho\left(\frac{x-x_0}{\sigma_x}\right)\left(\frac{y-y_0}{\sigma_y}\right)+\left(\frac{y-y_0}{\sigma_y}\right)^2\right]\right\}+B\,, \tag{10}$$

involves seven free parameters; the amplitude A, image center (x_0, y_0), the r.m.s. half-widths in x and y directions, σ_x and σ_y, the correlation coefficient ρ, and the constant B(cf. Chiu 1977; Auer and van Altena 1978). These parameters were determined by the least squares method. The image size is represented by

$$FWHM = 1.17(\sigma_x+\sigma_y)\,. \tag{11}$$

The value of FWHM for each plate is given in table 1 together with the seeing size estimated by eye at the observation. A comparison between FWHMs and eye-estimated seeing sizes indicates that the latter correspond to the diameter with 45 percent of the total intensity of a stellar image.

As we could not convolve individual frames with the appropriate point spread function due to the existence of the saturated part of the galaxy image, we stacked data without correction for the difference in image sizes. The stacked frames exhibited

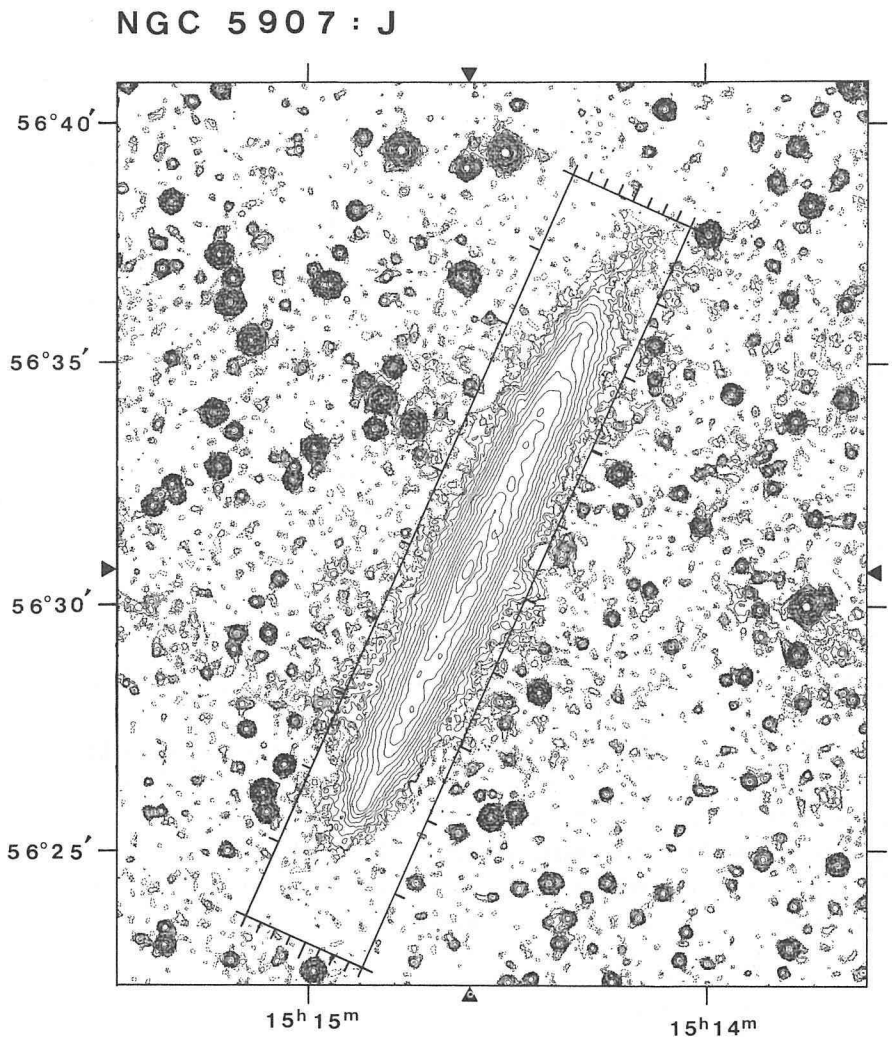

Figure 10. A contour map of the stacked data in *J* band. The box shows the region for the removal of stellar images around/in the galaxy. The longer side of the box is drawn parallel to the major axis of the galaxy. Tip marks indicate 100 arcsec along the major axis and 20 arcsec perpendicular to it. Contour levels are drawn with the faintest level of 27.64 mag arcsec^{-2} and a step of 0.5 mag arcsec^{-2}. Arrows in the margins indicate the position of the galactic center.

different star-image sizes of 6.6 arcsec and 5.0 arcsec FWHM for IIIa–J and IIIa–F, respectively. When the gaussian smoothing procedure was applied to the stacked frames, the difference in seeing size was taken into account: We applied gaussian weights with an FWHM of 5 arcsec and 7 arcsec to the IIIa–J and the IIIa–F image, respectively. The final image size resulted in 8.7 arcsec and 9.3 arcsec FWHM for the smoothed, stacked frame in each color band.

As we did not correct for the difference in image size in stacking, some errors should be introduced to the stacked images. We simulated the effects of various image

sizes by applying the gaussian smoothing with FWHMs of 5 arcsec and 7 arcsec to the same data to estimate differences in intensity of the galaxy image. Intensities differed about 0.1 mag around the dust lanes in the galactic plane, but there was little difference less than 0.05 mag in the other regions of the galaxy.

There are a few plates where the stellar images appeared elongated or doubled on the visual inspection of original plates. We estimated the direction and the axial ratio of their elongation in the seeing-correction procedure. We detected the maximum axial ratio of 2 for the plate KL3771. As the seeing size in this plate was relatively small compared with other plates, doubled images have been smoothed out during measurements and the smoothing process, and had no serious effect.

We estimated the total intensity, ΣI, of stellar images as

$$\Sigma I = 2\pi A \sigma_x \sigma_y (1-\rho^2)^{1/2} . \tag{12}$$

Ratios of ΣI between corresponding stars in one plate and the reference plate agreed with the ratio of the sky backgrounds, β, within 6 percent and 4 percent in J and F bands, respectively.

4-9. Photoelectric Calibration

The relative intensity was calibrated with the help of photoelectric aperture photometry. Tifft (1961, 1969) and de Vaucouleurs (1961) published the data of photoelectric photometries at 10 points in the galaxy NGC 5907. We summed up the intensity within an area of the same size of the aperture at the same position as they applied. Our pixel is of a square shape, while the apertures they used were of a circle. The intensity in the pixels near the edge of the aperture was summed partially within the aperture to improve photometric accuracy. Figure 11 shows the relation of the summed intensities to the corresponding photoelectric magnitudes. Our color bands J and F are related to Jonson's B and V bands by

$$\begin{aligned} J &= V+0.35(B-V) , \\ F &= V-0.69(B-V) , \end{aligned} \tag{13}$$

and

$$J-F = 1.04(B-V)$$

(Oemler 1974; Kirshner et al. 1978; Thuan and Gunn 1976; Kormendy and Bahcall 1974). The photoelectric magnitudes were converted into J and F bands with the relations (13).

Photoelectric magnitudes with apertures less than 30 arcsec deviate slightly from the straight line of the slope of 45 deg in figure 11. This seems to be caused by the difficulty to adjust the position of an aperture of a small size at the desired position. Thus the data for aperture sizes less than 30 arcsec were excluded in the calibration of the intensity. The straight lines shown in figure 11 were drawn to run through the photometric data points for apertures greater than 30 arcsec. Units of intensities of the stacked frames were estimated at 21.89 J mag arcsec^{-2} and 20.95 F mag arcsec^{-2} with deviation of 0.04 mag and 0.07 mag, respectively. These unit levels correspond to the

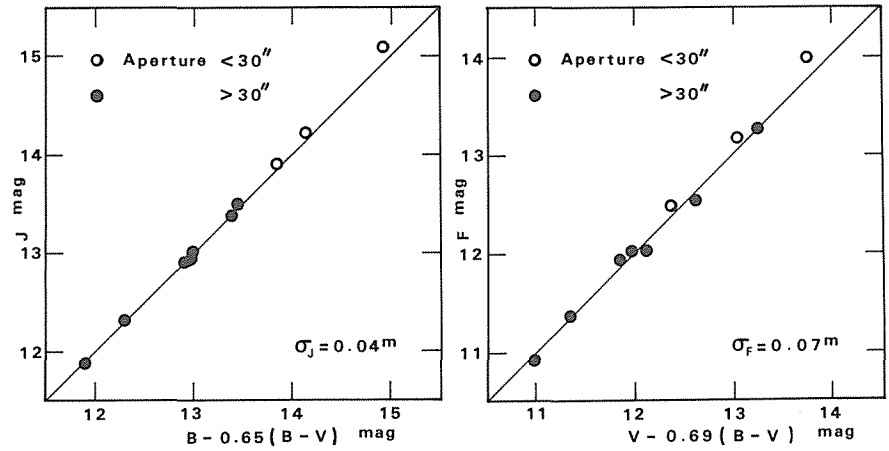

Figure 11. The calibration of the relative intensities using the photoelectric photometries with apertures of various sizes. The abscissa is the estimated brightness in J band (left) and in F band (right) from B and V photometry. The ordinate is the sum of the calibrated intensity within a given aperture. The straight line indicates the slope of unity. Centering errors could introduce the systematic deviations in photometry with apertures smaller than 30 arcsec in diameter. Data obtained with apertures greater than 30 arcsec were used to calibrate the photographic data.

extra-atmospheric sky brightness at the mean zenith distance (de Vaucouleurs 1975). The mean zenith distance was about 30 deg for our observations.

We then obtain the brightness distribution down to 27.64 J mag arcsec^{-2} and 26.70 F mag arcsec^{-2}, which correspond to 0.5 percent of the sky brightness. van der Kruit (1979) published the contour map of NGC 5907 down to 27.5 mag arcsec^{-2} in the similar color band to our J band. It is seen by comparison between our contour map in figure 10 and his figure 7 that the lowest level in our contour map is about 1 mag fainter than that of van der Kruit's. This difference in brightness agrees with a difference of zero levels in brightness by 0.86 mag between van der Kruit's and ours, as shown below, added by a difference in nominal brightness of the lowest level in contour maps by 0.14 mag.

5. Photometric Errors

Photographic photometry is subjected to various errors. Errors, which are introduced in certain processes, propagate to final data to deteriorate the photometric accuracy. Some errors are systematic in nature. These errors can be detected by comparing the data with those obtained by independent observations and/or methods. Errors of various types are introduced through image processing as described above; measuring errors such as instability of the system and drift of zero point in measurements, residuals in fitting of characteristic curves and in fitting of the sky background, errors introduced through translation of the frames to fit the positions, errors in ratios of intensity levels in stacking, and errors in photoelectric calibration. Procedures applied in fitting the sky can reduce errors introduced by the photographic treatments

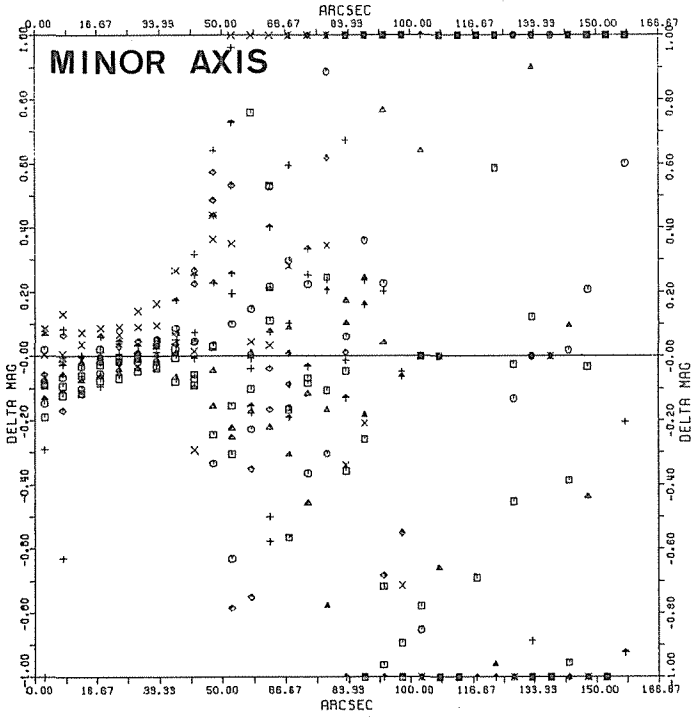
MINOR AXIS
ARCSEC
DELTA MAG
0.00
16.67
33.33
50.00
66.67
83.33
100.00
116.67
133.33
150.00
166.67
1.00
0.80
0.60
0.40
0.20
-0.00
-0.20
-0.40
-0.60
-0.80
-1.00

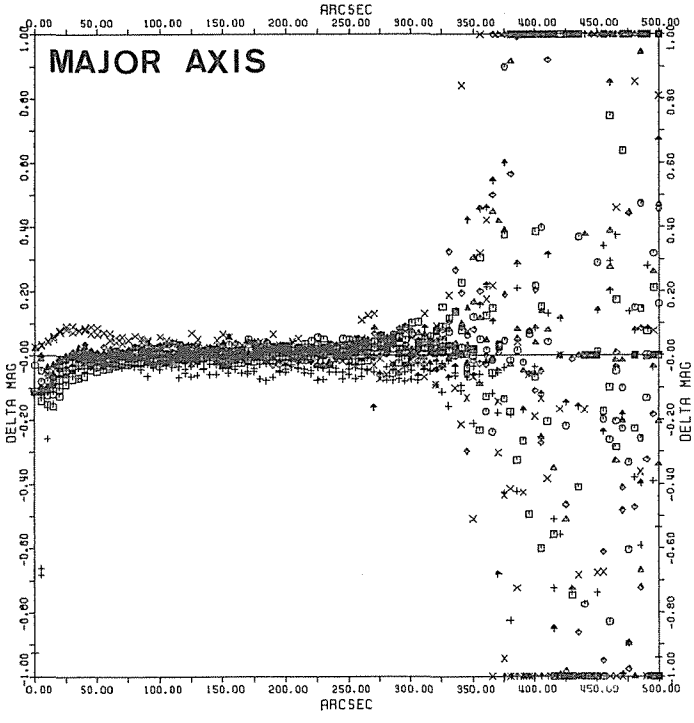
MAJOR AXIS
ARCSEC
DELTA MAG
0.00
50.00
100.00
150.00
200.00
250.00
300.00
350.00
400.00
450.00
500.00
1.00
0.80
0.60
0.40
0.20
-0.00
-0.20
-0.40
-0.60
-0.80
-1.00

and the measuring machine. Stacking of plates can suppress errors both of systematic and random natures.

Errors introduced by granularity were of the order of 0.02 D which corresponds to about 1.5 percent of the sky brightness. Residuals in fitting of the characteristic curves resulted in 0.02 in log I, i.e., 4.7 percent of the sky brightness. These are of systematic nature for each plate. Mismatch of positions by 4.0 μm might cause errors in intensity of the galaxy by the maximum of 4.1 percent of the galaxy brightness along the minor axis. This error is equivalent to 0.3 percent of the sky brightness at the level of 3 mag fainter than the sky. Errors introduced in fitting sky levels among plates were estimated at less than 6 percent and 4 percent of the sky brightness in J and F bands by using stellar photometry (section 4–8).

Systematic differences among plates were examined by drawing profiles along the major and the minor axis of the galaxy. Profiles were obtained by averaging the data every 5 arcsec over 5×20 arcsec^2 with the short side along each axis in J band. A difference of a profile of each frame from that of the stacked frame is plotted against the distance from the galactic center in figure 12, where different symbols correspond to different plates. In figure 13, the r.m.s. deviations of profiles from the stacked profile are shown against the distance from the center and against the surface brightness. We see from these figures that the luminosity distribution agrees to each other within ±0.05 mag except in the central region and outer faint parts. Large deviations in the center greater than 0.1 mag are over-estimated because the limitation of data with $(S/N)_{out}>40$ in stacking excluded the data which systematically deviate near the center in the deeply-exposed plates. Three plates were used to derive the stacked profile in the center as indicated in figure 12. The true error in the center is estimated as about 0.1 mag. In the regions more distant than r=325 arcsec (fainter than 24.5 mag arcsec^{-2}), errors increase rapidly to the r.m.s. deviation of 0.9 mag at the surface brightness 27.64 mag arcsec^{-2}. Stacking can reduce errors by an amount proportional to a square root of the number of plates (table 3), though level fitting in stacking introduces some errors. We stacked 6 deep IIIa–J plates and 7 deep IIIa–F plates. The accumulated errors in the stacked frames were of 0.04 mag or 3.9 percent of its brightness at the level brighter than μ_J=24.5 mag arcsec^{-2} and 0.46 mag or 53 percent of its brightness at 27.64 mag arcsec^{-2} in J band. The nearly constant errors in the bright levels are mainly due to systematic ones, though the large errors in the faint levels are of random nature to depend on the size of the used area, which we used of 5×20 arcsec^2, in examing the errors. These errors are compared to errors in the photoelectric calibration of 0.04 mag

Figure 12. Brightness differences between profiles obtained from the original data and the stacked, smoothed data along the major axis (lower panel) and the minor (upper panel) in J band. Brightness differences are shown in mag with zero at the horizontal line. The abscissa indicates the distance from the center in arcsec along the major and the minor axes. Profiles were obtained by averaging the data every 5 arcsec within an area of 5×20 arcsec^2 with the short side parallel to the axes. The systematic deviations appear in the central portion, but are fictitious because most of the central data of deeply exposed plates were not used due to the low S/N ratios. Abrupt increases of deviations occur beyond 325 arcsec and 42 arcsec along the major and the minor axis, respectively.

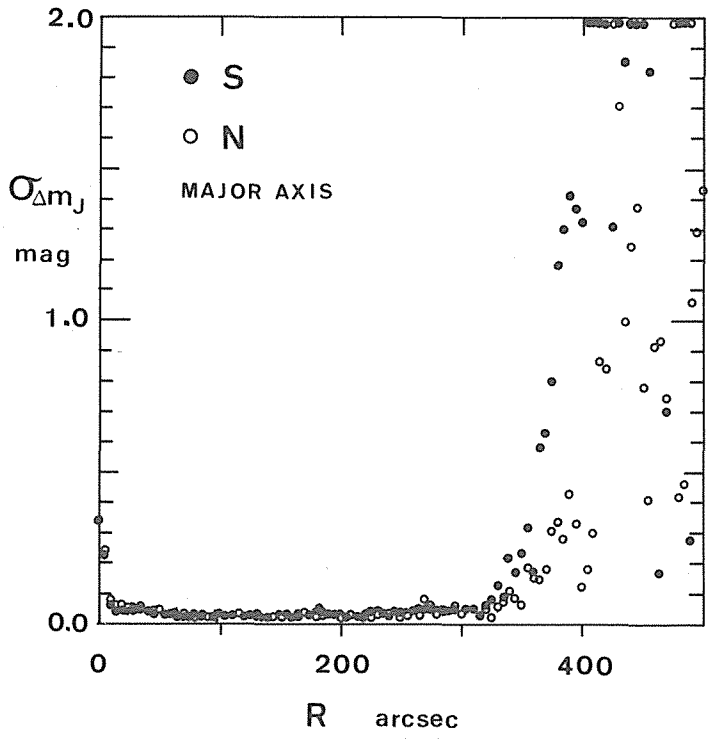

Figure 13 (a). The r.m.s. deviations of photometric data along the major axis as a function of the distance from the center in J band. The large deviations near the center are fictitious as noted in the caption of figure 12. Open and filled symbols show the northern and southern portions of the galaxy, respectively.

(3.8%) and 0.07 mag (6.7%) in J and F bands, respectively. When figure 13(b) is compared with figures 2 and 3 of van der Kruit's (1979), r.m.s. deviations of brightness show similar trends against the surface brightness. As the random noise and certain systematic errors were reduced by the stack of plates, we achieved an accuracy in the surface photometry of NGC 5907 at least 1.7 times as high as that of van der Kruit's.

We can estimate the systematic error in determination of the sky background by plotting the color $(J-F)$ against the surface brightness. An artificial shift of the sky level becomes evident in regions of low brightness; the brightness distribution shows the false cutoff in the outer faint portion (Capaccioli and de Vaucouleurs 1983; de Vaucouleurs 1948) and the color becomes systematically red or blue in the outer part of the galaxy. Figure 14 illustrates the color distribution against the surface brightness. Broken lines indicate the spread of colors if given systematic errors were introduced in one of the two color bands. Systematic deviations are not seen in figure 14. Plotted colors are scattered in the figure over the region where the data might be distributed in the case of the photometric error of 0.5 to 0.75 percent of the sky brightness. It does not conflict with a random noise of 0.5 percent attained after stacking.

The accuracy of an image processing system was examined by performing the surface photometry of the standard galaxy NGC 3379. The galaxy NGC 3379 was

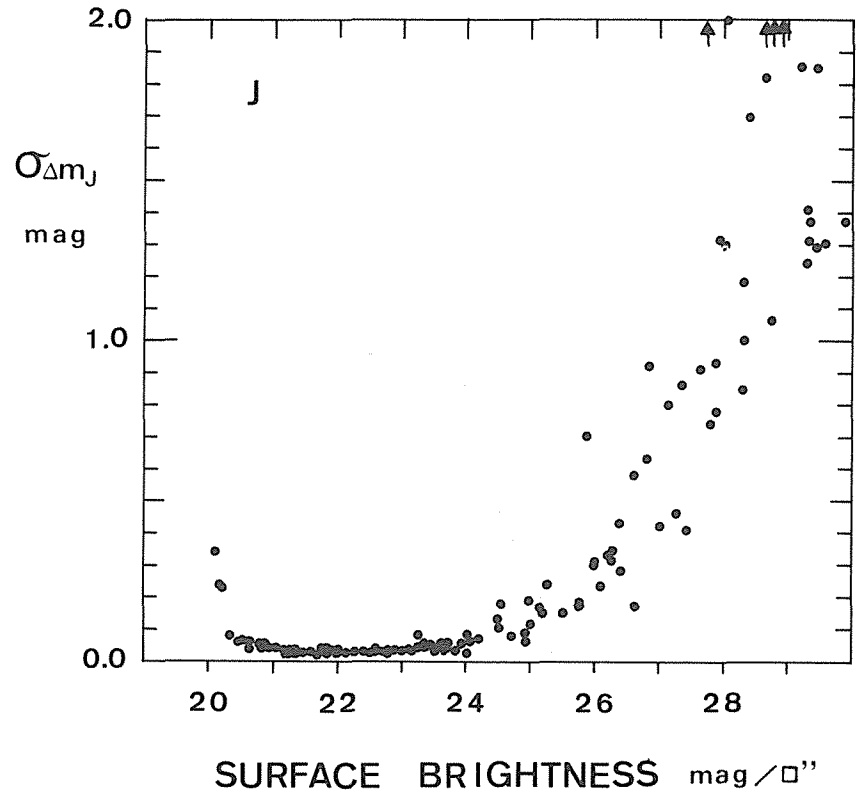

Figure 13 (b). The r.m.s. deviations of photometric data along the major axis as a function of the surface brightness in J band.

observed and processed with the same conditions and methods as those that NGC 5907 was treated with except stacking plates. We analyzed one plate of NGC 3379. The E–W profile is shown in figure 15, together with the standard profile of de Vaucouleurs and Capaccioli (1979). Our profile follows the standard profile with accuracy of 0.05 mag (4.7%) at the level brighter than 24.9 J mag arcsec^{-2} and 0.3 mag (32%) at 26.1 J mag arcsec^{-2}. We estimated the zero-point difference in brightness by shifting our profiles to coincide with the standard one. As the central part cannot be used due to the saturation, differential aperture photometry was also applied to the galaxy. The zero level in brightness agreed within 0.03 mag between our data and de Vaucouleurs and Capaccioli's standard data.

van der Kruit and Searle (1981) published the profiles of NGC 5907 at $z=20.4$ arcsec along the major axis, where z is the distance from the galactic plane. Their profiles were compared with our profiles in figure 16, which were obtained with the same binning size as van der Kruit and Searle had used. As there were some differences between their data and ours in the position of the galaxy center and in the position angle of the major axis, these two parameters were determined to yield the same differences in the central brightness between the northern and the southern profiles in their profiles and ours and to minimize differences in brightness along the

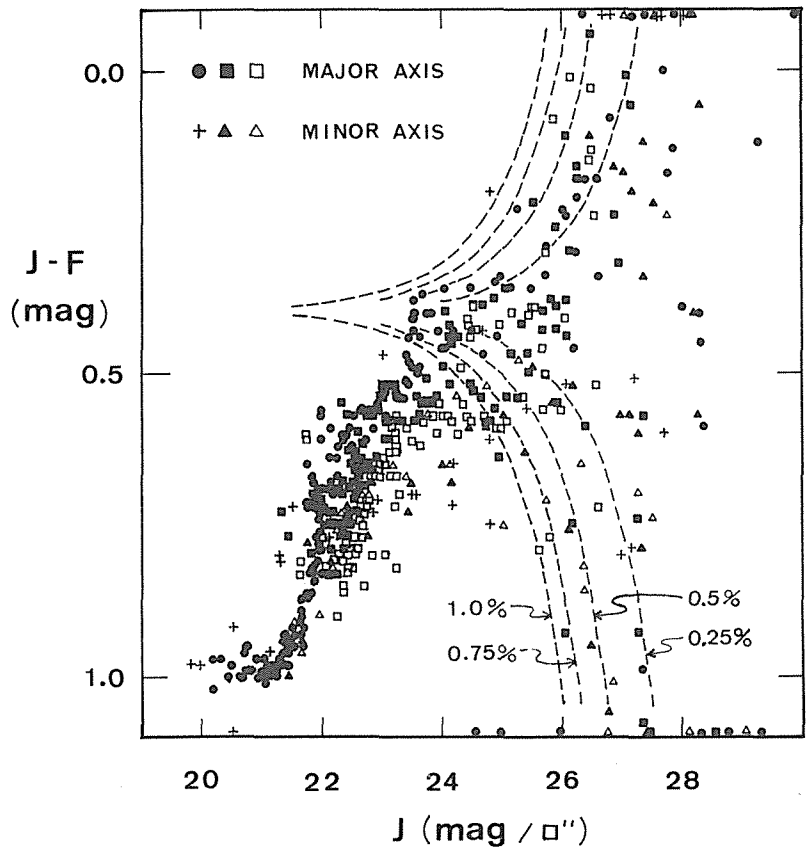

Figure 14. $(J-F)$ color distribution against the surface brightness parallel to the major and minor axes. The data are scattered in the low brightness level due to the background noises and the possible systematic error in determination of the sky level. Dotted curves show the range of scatters expected from the noises or errors of 0.25%, 0.5%, 0.75%, and 1.0% of the sky level.

whole profiles. The resulting difference was estimated as less than 0.2 mag at the brightness level of 22–25 mag arcsec^{-2} and less than 0.4 mag at 25–27 mag arcsec^{-2}. The zero level in brightness differed by about 0.86 mag arcsec^{-2}, which includes the correction of the sky brightness in van der Kruit and Searle's data by 0.2 mag (van der Kruit and Searle 1982).

6. Application of the Digital Surface Photometry to NGC 5907

The galaxy NGC 5907 manifests the conspicuous warp in the outer HI disk, though the galaxy is considered as an nearly isolated galaxy without companion galaxies which could approach to the galaxy during recent 10^9 years in the past. As the hypothesis had been commonly accepted that the tidal interaction by nearby companions could cause the warp (Hunter and Toomre 1969), Sancisi's (1976) discovery of the large HI warp in this galaxy was epoch-making. van der Kruit (1979) has performed a

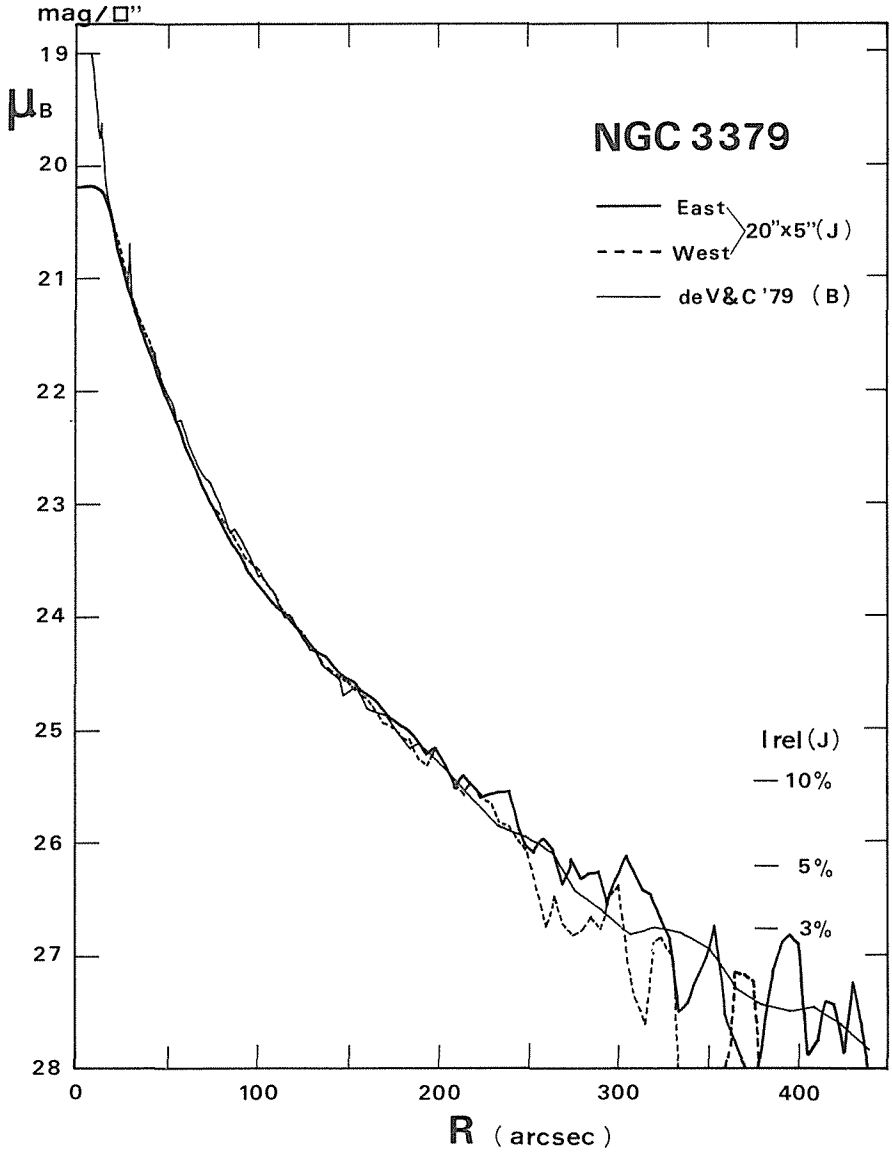

Figure 15. Luminosity profiles of the photometric standard galaxy NGC3379 along the east-west direction through the center. A photographic plate was processed by using nearly the same procedures as for NGC5907. Profiles were obtained by averaging the data every 5 arcsec within an area of 20×5 arcsec^2 with the short side along E-W direction. Our profiles are shifted to be compared with the standard profile. Except of the saturated central part, our profiles (thick lines) agree very well to the standard profile (a thin line). External photometric errors are estimated as 0.05 mag at $\mu_J<25$ and 0.3 mag at $\mu_J=26$.

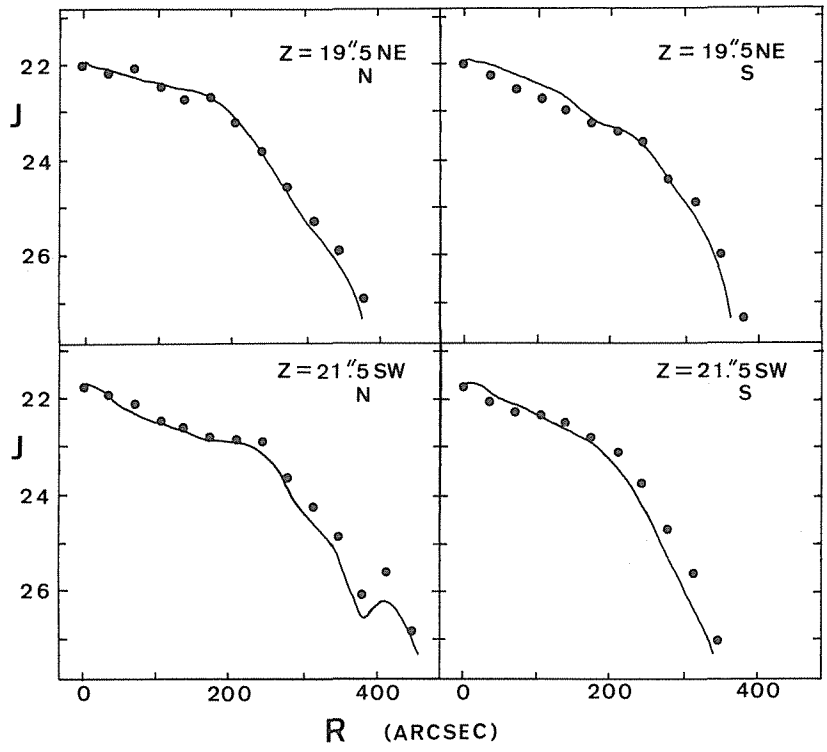

Figure 16. Comparison of profiles parallel to the major axis with those by van der Kruit and Searle (1981). Our profiles are indicated with dots and those by van der Kruit and Searle with lines. The positions and the position angles of our profiles were different from those of van der Kruit and Searle's in order to minimize the effect of errors in the position of the galaxy center and in the position angle of the major axis. Photometric differences are less than 0.2 mag at $\mu_J=22-25$ and less than 0.4 mag at $\mu_J=25-27$. A difference in zero-point is 0.86 mag.

surface photometry by using the Palomar 48 inch Schmidt telescope. He stacked two deep IIIa–J plates and achieved a photometry down to the faintest level of 27.5 mag arcsec^{-2}. He could detect the marginal hint of the warp in the outer stellar disk.

In order to confirm his marginal detection, we used now a total of thirteen deepest plates and two shortly-exposed plates taken at the Kiso Observatory during four seasons from 1979 to 1982. These plates were measured and analyzed by the method described in the previous section. Finally they were stacked to a composite intensity frame in each color band, *J* and *F*. The accuracy of the photometry was achieved to 0.04 mag at the level brighter than 24.5 *J* mag arcsec^{-2} and 0.46 mag at the faintest brightness of 27.64 *J* mag arcsec^{-2}. The lowest brightness we detected is 1.0 mag fainter than that of van der Kruit (1979), and the accuracy we achieved is 1.7 times higher. Detailed photometric data of NGC 5907 are derived from the composite frame in this paper. The detection of the warp in the stellar disk is discussed in a separate paper (Sasaki 1987).

Contour maps in *J* and *F* bands are shown in figure 10 and 17. The faintest levels

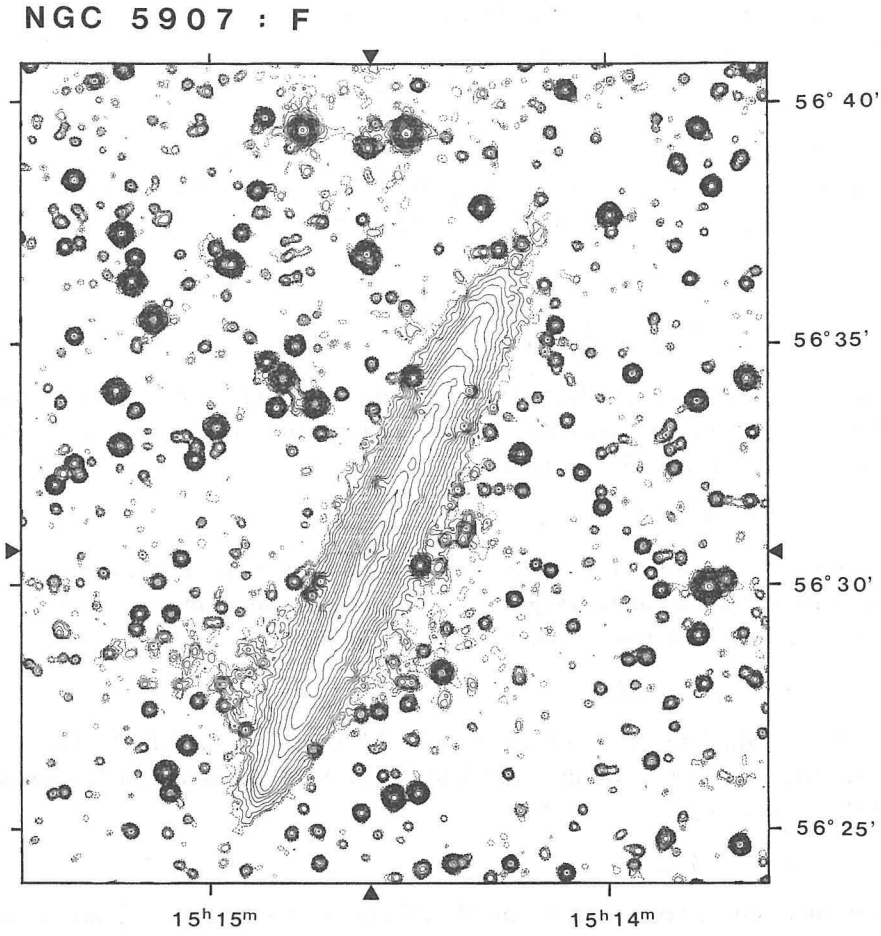

Figure 17. Contour map of the luminosity distribution of NGC5907 in F band. A faintest level (dotted lines) corresponds to $\mu_F=26.70$. Contours are drawn every 0.5 mag arcsec^{-2}.

correspond to the detection limits, i.e., 27.64 J mag arcsec^{-2} and 26.70 F mag arcsec^{-2}. A step of contours is 0.5 mag arcsec^{-2}. The brightest contour levels at the center of the galaxy are 19.64 J mag arcsec^{-2} and 18.70 F mag arcsec^{-2}.

There are many foreground stars which disturb photometric parameters to be derived. These stars were removed with the procedure described in section 4. The star removal was needed in the portion that was used to derive the photometric parameters (figure 10). There remain some traces of the removed stars, especially of bright stars. The sum of intensity of removed stars was about 9 percent of the total intensity of the galaxy. The remained intensity of the bright stars does not exceed a few percent of the star intensity. These traces can little affect the results concerning the photometric parameters.

The coordinates of the point with the maximum intensity in the galaxy were calculated as the nominal galactic center with regards to stars around the galaxy whose coordinates were quoted from the star catalog of the Smithonian Astrophysical

Observatory. An accuracy of the resulting coordinates was estimated as 0.5 arcsec. The coordinates obtained are given in table 6.

Photometric parameters in the de Vaucouleurs' system are derived from the stacked frame free of stellar images. According to de Vaucouleurs and Page (1962) and Tsikoudi (1977), the parameters are defined for an object having noncircular, irregular isophotes as follows: The differential brightness, ΔL_K, is defined as a sum of intensity with $I_K \leqq I < I_{k-1}$ for the k-th contour. The total (or asymptotic) luminosity is calculated as

$$L_T = \lim_{I_{min} \to 0} \sum_{I_k = I_{max}}^{I_{min}} \Delta L_k . \tag{14}$$

A small extrapolation toward $I_{min}=0$ is needed (de Vaucouleurs 1960), which amounted to about 1 percent of the total intensity of the galaxy. An equivalent radius as function of intensity, r^*, is defined by the relation

$$r^* = (A/\pi)^{1/2} , \tag{15}$$

where A is the total area enclosed by the isophotes of intensity I, including "islands". Mean luminosity distributions are given against the equivalent radius in figure 18. The relative integrated luminosity is obtained (figure 19) as

$$k(r^*) = L(r^*)/L_T , \tag{16}$$

where $L(r^*)$ is the integrated luminosity emitted between I_{max} and $I(r^*)$. The equivalent effective radius, r_e^*, within which half of the total luminosity of the galaxy is emitted, is defined by

$$k(r_e^*) = 1/2 . \tag{17}$$

The effective surface brightness, μ_e, and the effective surface intensity, I_e, are estimated

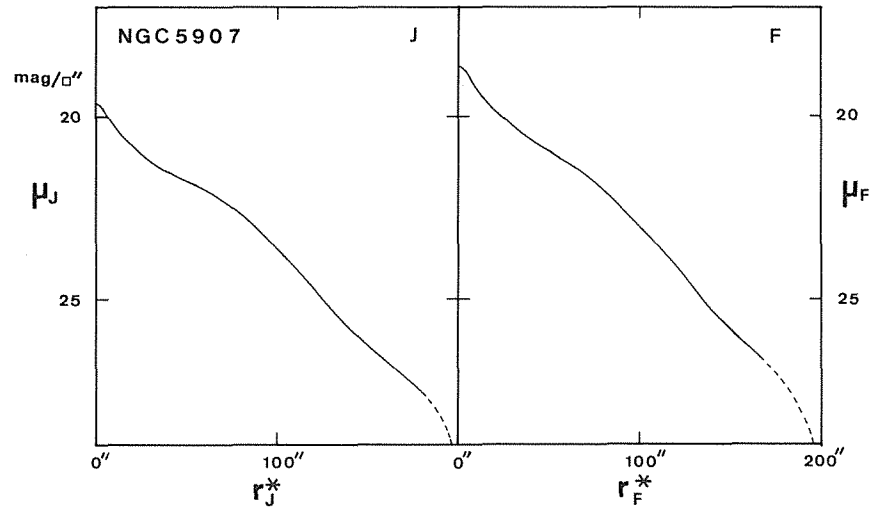

Figure 18. Mean luminosity distribution in NGC 5907 in J and F bands.

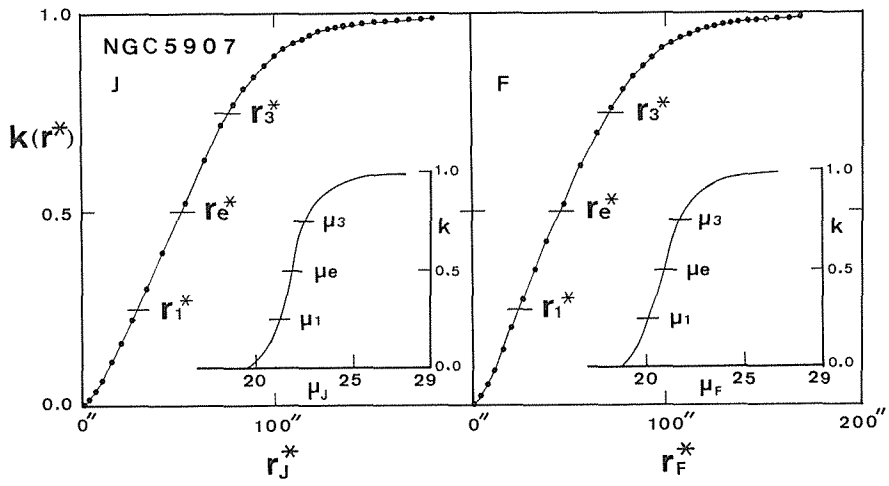

Figure 19. Relative integrated luminosity $k(r)$ versus equivalent radius r^* in J and F bands. The insets are $k(r)$ versus mean surface brightness (in mag arcsec^{-2}).

at r_e^*. The mean surface intensity, I_e', inside the effective radius is given by

$$I_e' = L_T/2\pi(r_e^*)^2 . \tag{18}$$

The mean surface brightness is

$$\mu_e' = M_T + 5\log r_e^* + 2.5\log(2\pi) . \tag{19}$$

Here M_T is the total magnitude of the galaxy.

The reduced variables, η and ρ^*, are used to describe the reduced mean luminosity profiles in J and F bands (tables 4 and 5):

$$\begin{aligned} \eta &= I/I_e , \\ \rho^* &= r^*/r_e^* . \end{aligned} \tag{20}$$

Additional dimensional parameters are defined as

$$\begin{aligned} k(r_1^*) &= 1/4 , \\ k(r_3^*) &= 3/4 . \end{aligned} \tag{21}$$

Two concentration indices are determined by

$$\begin{aligned} C_{21}^* &= r_e^*/r_1^* , \\ C_{32}^* &= r_3^*/r_e^* . \end{aligned} \tag{22}$$

The semi-major and semi-minor axes, a and b, are determined as the mean distance of pixels with intensity between I_{k-1} and I_k near the axes. Photometric parameters are derived based on the data within the box area shown in figure 10, free of stellar images. The derived parameters are not affected with reasonable tolerance in the size and the orientation of the box area.

We summarize the photometric parameters derived for NGC 5907 in table 6. The total magnitude of the galaxy, B_T, and color, $(B-V)_T$, are given as $B_T = 11.0$ mag and

Table 4. Mean J luminosity distribution in NGC 5907

μ	log I	ΔL	$\Sigma\Delta L$	A	r^*	$k(r^*)$	a	b/a	ρ	log η
19.64	0.9	0.018	0.018	0.002	1.589	0.002	0.476	2.606	0.031	0.859
19.89	0.8	0.154	0.171	0.024	5.271	0.020	3.775	0.465	0.101	0.759
20.14	0.7	0.173	0.344	0.055	7.946	0.040	7.157	0.478	0.153	0.659
20.39	0.6	0.234	0.578	0.108	11.124	0.067	11.542	0.488	0.214	0.559
20.64	0.5	0.405	0.983	0.223	15.970	0.114	20.605	0.357	0.307	0.459
20.89	0.4	0.406	1.389	0.368	20.536	0.162	31.722	0.285	0.395	0.359
21.14	0.3	0.504	1.893	0.595	26.112	0.220	46.856	0.214	0.502	0.259
21.39	0.2	0.689	2.582	0.983	33.560	0.300	65.718	0.192	0.646	0.159
21.64	0.1	0.792	3.374	1.551	42.164	0.393	94.711	0.156	0.811	0.059
21.89	0.0	1.093	4.467	2.525	53.796	0.520	138.905	0.129	1.035	−0.041
22.14	−0.1	0.933	5.400	3.566	63.921	0.628	174.939	0.118	1.230	−0.141
22.39	−0.2	0.752	6.152	4.626	72.805	0.716	208.101	0.112	1.401	−0.241
22.64	−0.3	0.472	6.624	5.459	79.090	0.771	234.689	0.104	1.522	−0.341
22.89	−0.4	0.336	6.961	6.208	84.343	0.810	247.928	0.106	1.623	−0.441
23.14	−0.5	0.276	7.237	6.984	89.458	0.842	260.176	0.107	1.721	−0.541
23.39	−0.6	0.245	7.482	7.854	94.869	0.871	282.811	0.107	1.825	−0.641
23.64	−0.7	0.203	7.685	8.758	100.177	0.894	296.373	0.107	1.927	−0.741
23.89	−0.8	0.161	7.846	9.661	105.218	0.913	308.554	0.108	2.024	−0.841
24.14	−0.9	0.126	7.972	10.549	109.948	0.928	315.016	0.113	2.115	−0.941
24.39	−1.0	0.101	8.072	11.442	114.505	0.939	323.851	0.117	2.203	−1.041
24.64	−1.1	0.079	8.151	12.326	118.844	0.949	334.816	0.119	2.286	−1.141
24.89	−1.2	0.066	8.217	13.251	123.226	0.956	339.727	0.130	2.371	−1.241
25.14	−1.3	0.053	8.270	14.183	127.487	0.962	348.491	0.148	2.453	−1.341
25.39	−1.4	0.044	8.314	15.173	131.858	0.968	349.630	0.161	2.537	−1.441
25.64	−1.5	0.035	8.349	16.156	136.062	0.972	353.959	0.161	2.618	−1.541
25.89	−1.6	0.031	8.379	17.235	140.536	0.975	361.712	0.159	2.704	−1.641
26.14	−1.7	0.028	8.407	18.489	145.558	0.978	365.110	0.165	2.800	−1.741
26.39	−1.8	0.026	8.433	19.944	151.175	0.981	372.695	0.162	2.908	−1.841
26.64	−1.9	0.023	8.456	21.572	157.226	0.984	379.453	0.171	3.025	−1.941
26.89	−2.0	0.019	8.475	23.302	163.409	0.986	394.308	0.160	3.144	−2.041
27.14	−2.1	0.016	8.491	25.109	169.627	0.988	413.242	0.143	3.263	−2.141
27.39	−2.2	0.013	8.504	26.932	175.675	0.990	439.100	0.143	3.380	−2.241
27.64	−2.3	0.009	8.513	28.574	180.950	0.991	436.202	0.135	3.481	−2.341

Notes: μ in J mag arcsec^{-2}, I in arbitrary intensity units, L in J mag, A in arcmin^2, r^* in arcsec, and a in arcsec. $\rho=r^*/r_e^*$ and log $\eta=\log(I/I_e)$; $\eta=1$ for $\mu=\mu_e=21.79$.

$(B-V)_T=0.77$ in $RC2$. They are converted to our color bands; $J_T(RC2)=10.50$, $F_T(RC2)=9.70$, and $(J-F)_T(RC2)=0.80$. These values coincide fairly well with our estimation, leaving small differences of $\Delta J=0.17$ mag, $\Delta F=0.17$ mag, and $\Delta(J-F)=0.0$ mag.

Figure 20 shows axial ratios as a function of the semi-major axis a. The axial ratio tends toward $b/a\sim0.5$ in the nuclear region, where the strong extinction by the dust lane may hide a half of the bulge. The ratio decreases to $b/a=0.15$ at $a=105$ arcsec. In the region of $3'<a<5'$ the mean axial ratios become 0.11 with an r.m.s. deviation of 0.004 both in J and F bands.

The true axial ratio of disk galaxies seen exactly edge-on has been considered to be 0.2 (Holmberg 1946). Some galaxies of type Sc have the axial ratios smaller than 0.2 and NGC 5907 is one of the flattest system among Sc galaxies (Heidmann et al. 1972). Some galaxies of type Sd have axial ratios even close to 0.05 (Goad and Roberts 1981). The inclinations of galaxies have been often calculated by assuming the true axial ratio

Table 5. Mean F luminosity distribution in NGC 5907

μ	log I	ΔL	$\Sigma\Delta L$	A	r^*	$k(r^*)$	a	b/a	ρ	log η
18.70	0.9	0.018	0.018	0.002	1.589	0.002	0.476	2.606	0.034	0.857
18.95	0.8	0.188	0.206	0.029	5.730	0.027	3.384	0.615	0.124	0.757
19.20	0.7	0.220	0.426	0.068	8.848	0.056	7.950	0.445	0.191	0.657
19.45	0.6	0.264	0.690	0.128	12.102	0.091	14.610	0.439	0.261	0.557
19.70	0.5	0.398	1.088	0.240	16.591	0.144	21.388	0.346	0.358	0.457
19.95	0.4	0.443	1.531	0.399	21.379	0.203	34.864	0.269	0.461	0.357
20.20	0.3	0.537	2.068	0.641	27.108	0.274	50.453	0.205	0.585	0.257
20.45	0.2	0.577	2.645	0.965	33.258	0.350	67.771	0.182	0.718	0.157
20.70	0.1	0.547	3.191	1.355	39.409	0.422	85.966	0.162	0.850	0.057
20.95	0.0	0.707	3.898	1.990	47.753	0.516	115.134	0.149	1.030	−0.043
21.20	−0.1	0.740	4.638	2.827	56.921	0.614	157.336	0.124	1.228	−0.143
21.45	−0.2	0.616	5.254	3.696	65.076	0.695	184.829	0.113	1.404	−0.243
21.70	−0.3	0.505	5.759	4.590	72.527	0.762	211.888	0.112	1.565	−0.343
21.95	−0.4	0.361	6.120	5.393	78.609	0.810	231.335	0.108	1.696	−0.443
22.20	−0.5	0.249	6.369	6.096	83.576	0.843	243.240	0.107	1.803	−0.543
22.45	−0.6	0.202	6.571	6.814	88.364	0.869	253.349	0.112	1.907	−0.643
22.70	−0.7	0.162	6.733	7.537	92.933	0.891	265.143	0.114	2.005	−0.743
22.95	−0.8	0.149	6.882	8.376	97.973	0.911	283.402	0.115	2.114	−0.843
23.20	−0.9	0.121	7.003	9.229	102.839	0.927	298.886	0.110	2.219	−0.943
23.45	−1.0	0.101	7.104	10.124	107.709	0.940	309.118	0.117	2.324	−1.043
23.70	−1.1	0.076	7.179	10.975	112.143	0.950	316.683	0.122	2.420	−1.143
23.95	−1.2	0.064	7.243	11.874	116.646	0.958	325.946	0.119	2.517	−1.243
24.20	−1.3	0.049	7.292	12.749	120.867	0.965	333.032	0.128	2.608	−1.343
24.45	−1.4	0.040	7.332	13.643	125.036	0.970	340.930	0.132	2.698	−1.443
24.70	−1.5	0.032	7.364	14.534	129.052	0.974	347.143	0.130	2.785	−1.543
24.95	−1.6	0.026	7.390	15.446	133.041	0.978	348.622	0.138	2.871	−1.643
25.20	−1.7	0.021	7.411	16.396	137.070	0.980	354.532	0.160	2.958	−1.743
25.45	−1.8	0.019	7.430	17.469	141.485	0.983	358.222	0.171	3.053	−1.843
25.70	−1.9	0.018	7.447	18.721	146.466	0.985	362.882	0.162	3.160	−1.943
25.95	−2.0	0.014	7.461	19.972	151.284	0.987	364.957	0.158	3.264	−2.043
26.20	−2.1	0.014	7.475	21.575	157.234	0.989	380.005	0.160	3.393	−2.143
26.45	−2.2	0.012	7.487	23.274	163.308	0.991	401.016	0.144	3.524	−2.243
26.70	−2.3	0.009	7.496	24.810	168.611	0.992	406.624	0.142	3.638	−2.343

Notes: μ in Fmag arcsec^{-2}, I in arbitrary intensity units, L in F mag, A in arcmin^2, r^* in arcsec, and a in arcsec. $\rho=r^*/r_e^*$ and $\log\eta=\log(I/I_e)$; $\eta=1$ for $\mu=\mu_e=20.84$.

of 0.2 for all disk galaxies and the inclination of NGC 5907 was estimated as $i=87°$ (Roberts 1969, 1975). It is worth to note that the existence of flat galaxies with an axial ratio less than 0.2 introduces some errors in the inclinations calculated under the assumption of the intrinsic ratio of $b/a=0.2$ as noted by Heidmann et al. (1972). For NGC 5907, we now obtain the inclination of 88° by using the intrinsic axial ratio of Sc galaxies derived by Heidmann et al (1972).

In order to examine the optical warp clearly, the vertical profiles perpendicular to the major axis are drawn every 50 arcsec in r. They are obtained by averaging intensities every 5 arcsec within an area of 5×20 arcsec^2 parallel and perpendicular to the minor axis. Profiles are shown for the portion brighter than 28 mag arcsec^{-2}. They are fairly symmetric about the galactic plane as indicated by van der Kruit and Searle (1981). Each profile is reversed around the major axis and is drawn together with the reversed one in figure 21. The systematic shift between the reversed and the original profiles, if any, is interpreted as indication of the warp, which is discussed in the

Table 6. Photometric parameters of NGC 5907

Right ascension (1950)[1]	α	$15^h\ 14^m\ 35.81^s$	
Declination (1950)[1]	δ	56° 30′ 42.5″	
Galactic coordinate	l, b	91.58°, 51.09°	
Type[2]		SA(s)c:sp	
Apparent distance modulus	m−M	30.21	
Geometric distance adopted	Δ	11.0 Mpc (3.20 kpc arcmin^{-1})	
		J-band	F-band
Total apparent magnitude	m_T	10.67	9.87
Absolute magnitude	M_T	−19.54	−20.34
Absolute luminosity	$\log L/L_\odot$	9.84	9.89
Major axis position angle		156°	
Mean axis ratio	$\langle b/a \rangle$	0.109 (2′.92<a<5′.25)	0.112 (3′.08<a<5′.15)
Inclination	i	88°	
Observed peak brightness	μ_0 L_0 ($L_\odot$ pc^{-2})	19.64 628.8	18.65 836.7
The threshold surface brightness	μ_m L_m ($L_\odot$ pc^{-2})	27.64 0.40	26.70 0.50
Major axis at threshold	$2a_m$	14.540′ 46.52 kpc	13.554′ 43.37 kpc
Minor axis at threshold	$2b_m$	1.961′ 6.27 kpc	1.919′ 6.14 kpc
Major axis at μ=25 mag arcsec^{-2}	$2a_{25}$	11.453′ 36.65 kpc	11.660′ 37.31 kpc
Minor axis at μ=25 mag arcsec^{-2}	$2b_{25}$	1.582′ 5.06 kpc	1.662′ 5.32 kpc
Luminosity within μ=25 mag arcsec^{-2}	k_{25}	0.959	0.978
Parameters at k=1/4			
Semimajor axis	a_1	0.869′ 2.78 kpc	0.737′ 2.36 kpc
Axis ratio	q_1	0.207	0.230
Equivalent radius	r_1^*	0.481′ 1.54 kpc	0.420′ 1.34 kpc
Surface brightness	μ_1 L_1 ($L_\odot$ pc^{-2})	21.21 148.1	20.10 220.1
Parameters at k=1/2 (effective)			
Semimajor axis	a_e	2.020′ 6.46 kpc	1.705′ 5.46 kpc
Axis ratio	q_e	0.140	0.155
Equivalent radius	r_e^*	0.866′ 2.77 kpc	0.772′ 2.47 kpc
Surface brightness	μ_e L_e ($L_\odot$ pc^{-2})	21.79 86.8	20.84 111.3
Mean surface brightness	μ_e' L_e ($L_\odot$ pc^{-2})	21.24 144.1	20.19 202.6
Parameters at k=3/4			
Semimajor axis	a_3	3.752′ 12.01 kpc	3.459′ 11.07 kpc
Axis ratio	q_3	0.107	0.113

Equivalent radius	r_3^*	1.278′ 4.09 kpc	1.186′ 3.79 kpc
Surface brightness	μ_3 L_3 ($L_\odot$ pc^{-2})	22.55 43.1	21.66 52.3
Concentration indices	$C_{21}=r_e^*/r_1^*$ $C_{32}=r_3^*/r_e^*$	1.800 1.476	1.838 1.536

[1] Position at the maximum intensity, [2] From the RC2.

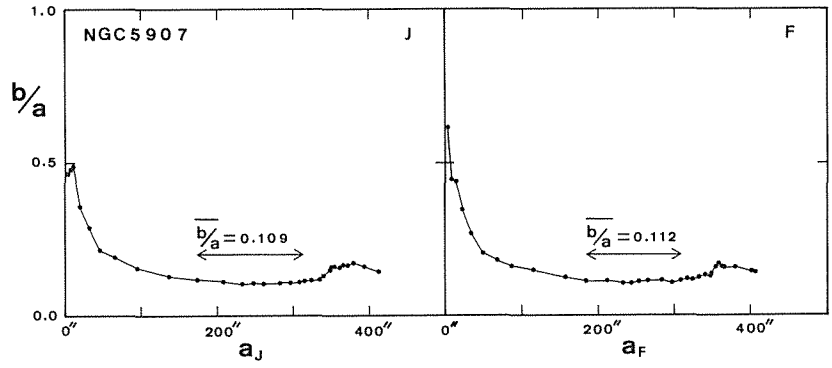

Figure 20. Axial ratios, b/a, along the major axis versus the mean semimajor axis, a, of isophotes in J and F bands. Horizontal lines show the ranges where the mean axial ratios are obtained.

separate paper (Sasaki 1987).

7. Summary

(1) Obsevations were done with the 105 cm Kiso Schmidt telescope. The plates were exposed to achieve the density level of the maximum DQE in order to detect the faint outskirt of the galaxy.

(2) We can measure plates with an accuracy of 0.01 D with the measuring machine Joyce-Loebl MDM6. A positional accuracy of 2 μm and a spatial resolution of 10 μm are achievable. The machine needs a warming-up time of typically 3 hours. A short depth-of-focus would have some effects on measurements, but it compares to the drift of the intrinsic density scale of the machine.

(3) We summarize procedures for the image processing of the photographic plates in a flow chart (figure 22). We analyzed the plates and stacked them to achieve the photometric accuracy of about 0.04 mag at levels brighter than 24.5 J mag arcsec^{-2}. For the faintest level of 1 σ of the sky brightness, μ_J=27.64 mag arcsec^{-2}, we achieved the photometric accuracy 0.46 mag by stacking. Systematic errors can be less than 0.75 percent of the sky brightness. A comparison of the profile of the standard galaxy NGC 3379 with that of de Vaucouleurs and Capaccioli's indicates that photometry was performed in one plate with accuracy higher than 0.3 mag down to the level of 26.1 J mag arcsec^{-2}.

(4) The surface photometry of NGC 5907 was performed in J and F bands using seven

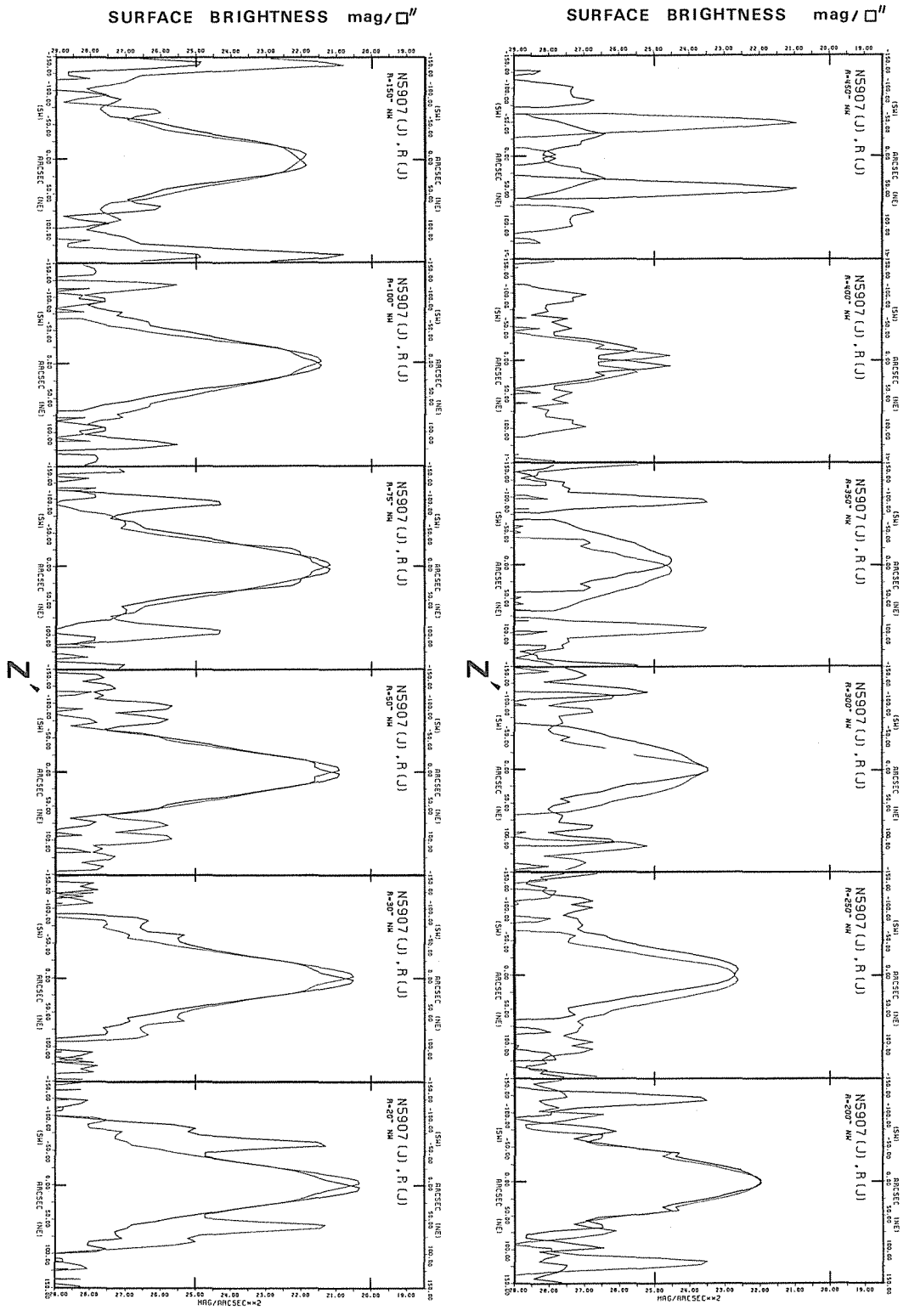
SURFACE BRIGHTNESS mag/□″
N5907(J),R(J)
R=450″ NW
R=400″ NW
R=350″ NW
R=300″ NW
R=250″ NW
R=200″ NW
MAG/ARCSEC**2
SURFACE BRIGHTNESS mag/□″
N5907(J),R(J)
R=150″ NW
R=100″ NW
R=75″ NW
R=50″ NW
R=30″ NW
R=20″ NW
MAG/ARCSEC**2

Figure 21 (a).

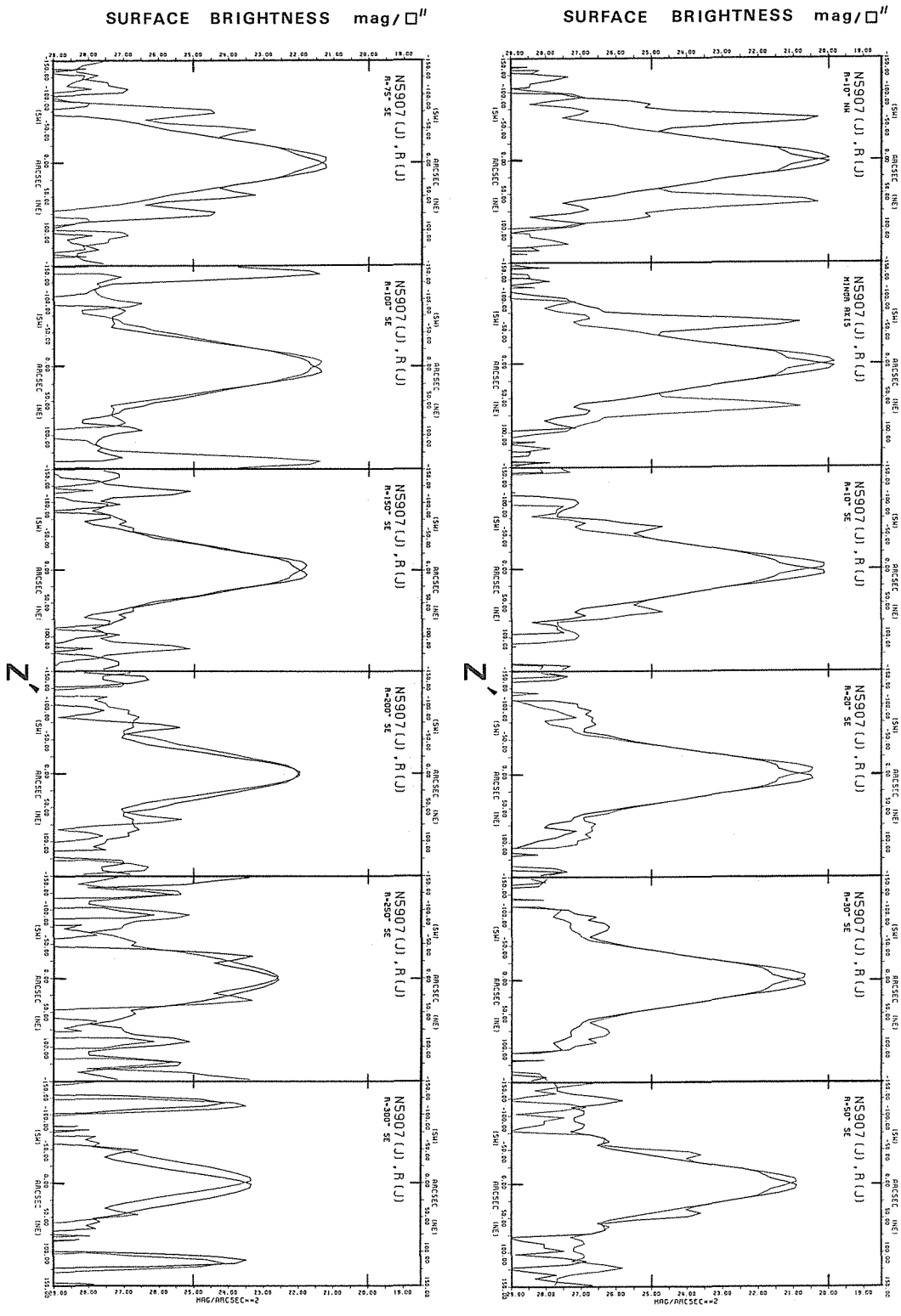
SURFACE BRIGHTNESS mag/□″
N5907 (J) , R (J)
R=10" NW
MINOR AXIS
R=10" SE
R=20" SE
R=30" SE
R=90" SE
R=75" SE
R=100" SE
R=150" SE
R=200" SE
R=250" SE
R=300" SE
ARCSEC (NE)
MAG/ARCSEC**2
N

Figure 21 (b).

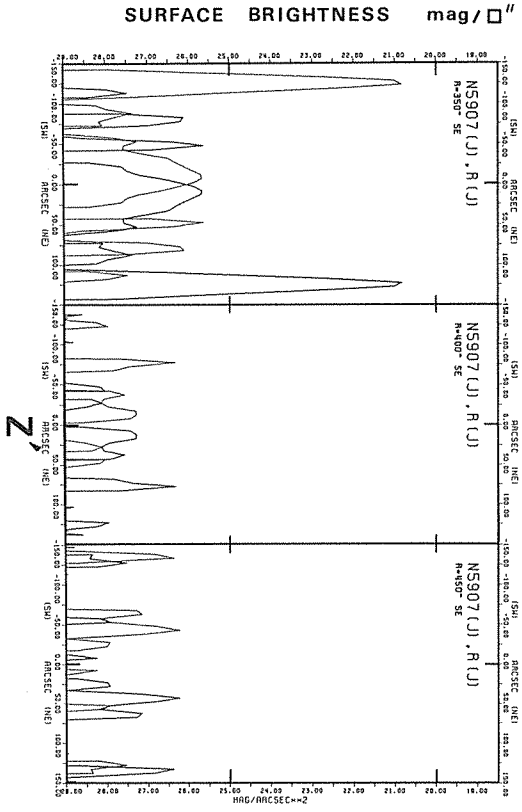

Figure 21 (c).

Figure 21. Superposition of every luminosity profile parallel to the minor axis (thick line) and its reversed profile (thin line). Profiles are shown at the distance from the galactic center along the major axis $r=0''$, $\pm 10''$, $\pm 20''$, $\pm 30''$, $\pm 50''$, $\pm 75''$, $\pm 100''$, $\pm 150''$, $\pm 200''$, $\pm 250''$, $\pm 300''$, $\pm 350''$, $\pm 400''$, and $\pm 450''$. The abscissa z' is the distance from the axis parallel to the major axis and shifted by $2.5''$ from the major axis. The profiles show fairly symmetric with regard to the major axis for r ‹ 200 arcsec. Beyond there they deviate from symmetry to manifest the warp in the outer part.

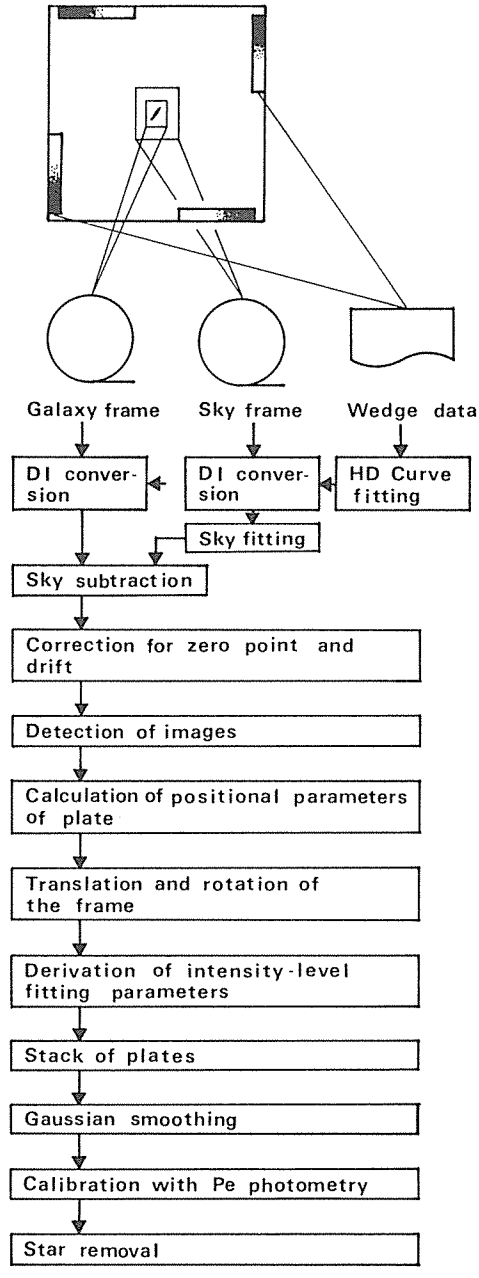

Figure 22. A flow chart of image processing.

and eight deeply-exposed plates, respectively. Photometric parameters were derived in a conventional manner. Photometric data are presented in tabular and graphic forms according to de Vaucouleurs' system. Vertical profiles are drawn with their reversed ones to investigate the warp of the galactic disk.

Acknowledgements

The author expresses his hearty thanks to Prof. B. Takase, Prof. K. Ishida, Dr. H. Maehara, Dr. S. Okamura, and other staff members at the Kiso Observatory for making the telescope and the facilities available to him and for their kind hospitality. This work has been successfully carried out with their invaluable cooperation. The author is also indebted to Prof. T. Kogure, Dr. H. Ohtani, and other staff members and the collaborators at the Department of Astronomy, University of Kyoto for their discussions and encouragements. He also describes his hearty thanks to Prof. K. Kodaira for his discussions and encouragements and for critical reading of the manuscript. The author expresses his deep gratitude to his wife, Mrs. K. Sasaki, for her devoted supports. Numerical calculations were done mainly with FACOM computers at the Kyoto University Computer Center.

This paper is based on the author's dissertation submitted to the University of Tokyo, in partial fulfillment of the requirements for the doctorate.

References

Ables, H. D. 1971, *Publ. U. S. Naval Obs. 2nd Ser.*, Vol. XX, Part IV.
Aoki, T. 1982, *Tokyo Astron. Obs. Report*, **19**, 567.
Arp, H. 1977, *Astrophys. J.*, **218**, 70.
Arp, H., and Lorre, J. 1976, *Astrophys. J.*, **210**, 58.
Auer, L. H., and van Altena, W. F. 1978, *Astron. J.*, **83** 531, (Erratum: *ibid.*, **83**, 1468).
Barbon, R., Benacchio, L., and Capaccioli, M. 1976, *Astron. Astrophys.*, **51**, 25.
Benedict, G. F. 1976, *Astron. J.*, **81**, 89.
Binggeli, B., Sandage, A., and Tammann, G. A. 1985, *Astron. J.*, **90**, 1681.
Binggeli, B., Sandage, A., and Tarenghi, M. 1984, *Astron. J.*, **89**, 64.
Blackman, C. P. 1979, *Mon. Not. R. Astron. Soc.*, **186**, 701.
Boroson, T. 1981, *Astrophys. J. Suppl.*, **46**, 177.
Burstein, D. 1979, *AAS Photo-Bull.*, No. 20, 6.
Capaccioli, M., and de Vaucouleurs, G. 1983, *Astrophys. J. Suppl.*, **52**, 465.
Chiu, L.-T. G. 1977, *Astron. J.*, **82**, 842.
Davoust, E., and Pence, W. 1982, *Astron. Astrophys. Suppl.*, **49**, 631.
de Vaucouleurs, G. 1948, *Ann. d'Astrophys.*, **11**, 247.
de Vaucouleurs, G. 1960, *Astrophys. J.*, **131**, 574.
de Vaucouleurs, G. 1961, *Astrophys. J. Suppl.*, **5**, 233.
de Vaucouleurs, G. 1968, *App. Opt.*, **7**, 1513.
de Vaucouleurs, G. 1975, *Astrophys. J. Suppl.*, **29**, 193.
de Vaucouleurs, G., and Capaccioli, M. 1979, *Astrophys. J. Suppl.*, **40**, 699.
de Vaucouleurs, G., and Page, J. 1962, *Astrophys. J.*, **136**, 107.
de Vaucouleurs, G., de Vaucouleurs, A., and Corwin, H. G., Jr. 1976, *Second Reference Catalogue of Bright Galaxies.*
Fraser, G. W. 1977, *Astron. Astrophys. Suppl.*, **29**, 161.
Furenlid, I. 1978, in *Modern Techniques in Astronomical Photography*, eds. R. M. West, J. L. Heudier (ESO, Geneva), p. 153.
Goad, J. W., and Roberts, M. S. 1981, *Astrophys. J.*, **250**, 79.
Heidmann, J., Heidmann, N., and de Vaucouleurs, G. 1972, *Mem. R. Astron. Soc.*, **75**, 85.
Holmberg, E. 1946, *Medd. Lunds Astron. Obs., Ser. II*, No. 117.
Hunter, C., and Toomre, A. 1969, *Astrophys. J.* **155**, 747.

Ishida, K. 1978, in *Proc. Schmidt Symp.*, p. 49.
Jones, W. B., Obitts, D. L., Gallet, R. M., and de Vaucouleurs, G. 1967, *Publ. Dept. Astron. Univ. Texas, Ser.* 2, Vol. 1, No. 8.
Kirshner, R. P., Oemler, A., Jr., and Schechter, P. L. 1978, *Astron. J.*, **83**, 1549.
Kormendy, J. 1973, *Astron. J.*, **78**, 255.
Kormendy, J. 1977, *Astrophys. J.*, **214**, 359.
Kormendy, J., and Bahcall, J. N. 1974, *Astron. J.*, **79**, 671.
Lorre, J. 1978, *Astrophys. J. Lett.*, **222**, L99.
Maehara, H. 1981, *AAS Photo-Bull.*, No. 26, 14.
Nieto, J.-L. 1984, *New Aspects of Galaxy Photometry* (Springer-Verlag, Berlin).
Oemler, A., Jr. 1974, *Astron. J.*, **194**, 1.
Okamura, S. 1977, *Annals Tokyo Astron. Obs.*, *2nd Ser.*, Vol. XVI, No. 3.
Pence, W. D. 1978, *Publ. Astron. Univ. Texas*, No. 14 (1980, *Astrophys. J.*, **239**, 54).
Roberts, M. S. 1969, *Astron. J.*, **74**, 859.
Roberts, M. S. 1975, in *Galaxies and the Universe* (University of Chicago Press, Chicago), Chap. 9, p. 309.
Sancisi, R. 1976, *Astron. Astrophys.*, **53**, 159.
Sasaki, T. 1983, *AAS Photo-Bull.*, No. 32, 3.
Sasaki, T. 1987, *Publ. Astron. Soc. Japan.*, **39**, 849.
Schweizer, F. 1976, *Astrophys. J. Suppl.*, **31**, 313.
Sedmak, G., Capaccioli, M., and Allen, R. J. 1979, *Image Processing in Astronomy.* (Osservatorio Astronomico di Trieste).
Sewell, M. H. 1975, *AAS Photo-Bull.*, No. 8, p. 3.
Simkin, S. M. 1975, *Astron. J.*, **80**, 415.
Smith, A. G., and Hoag, A. A. 1979, *Ann. Rev. Astron. Astrophys.*, **17**, 43.
Strom, K. M., and Strom, S. E. 1978, *Astron. J.*, **83**, 73.
Takase, B., Ishida, K., Shimizu, M., Maehara, H., Hamajima, K., Noguchi, T., and Ohashi, M. 1977, *Ann. Tokyo Astron. Obs. 2nd Ser.*, Vol. XVI, No. 2, 74.
Thuan, T. X., and Gunn, J. E. 1976, *Publ. Astron. Soc. Pacific*, 88, 543.
Tifft, W. G. 1961, *Astron. J.*, **66**, 390.
Tifft, W. G. 1969, *Astron. J.*, **74**, 354.
Tsikoudi, V. 1977, *Publ. Astron. Univ. Texas*, No. 10 (1979, Astrophys. J., **234**, 842).
Tsubaki, T., and Engvold, O. 1975, *AAS Photo-Bull.*, No. 9, p. 17.
van der Kruit, P. C. 1979, *Astron. Astrophys. Suppl.*, **38**, 15.
van der Kruit, P. C., and Searle, L. 1981, *Astron. Astrophys.*, **95**, 105.
van der Kruit, P. C., and Searle, L. 1982, *Astron. Astrophys.*, **110**, 61.
Watanabe, M. 1982, *Annals Tokyo Astron. Obs. 2nd Ser.*, Vol. XIX, No. 2.
Woolf, N. J. 1982, *Ann. Rev. Astron. Astrophys.*, **20**, 367.